International Journal of Plasticity 153 (2022) 103292

Contents lists available at ScienceDirect

International Journal of Plasticity

journal homepage: www.elsevier.com/locate/ijplas

Experimental characterization and crystal plasticity modeling for predicting load reversals in AA6016-T4 and AA7021-T79

Sowmya Daroju [a], Toshihiko Kuwabara [b], Rishabh Sharma [c], David T. Fullwood [c], Michael P. Miles [d], Marko Knezevic [a,*]

[a] Department of Mechanical Engineering, University of New Hampshire, Durham, NH 03824, USA
[b] Division of Advanced Mechanical Systems Engineering, Institute of Engineering, Tokyo University of Agriculture and Technology, Tokyo 184-8588, Japan
[c] Department of Mechanical Engineering, Brigham Young University, Provo, UT 84602, USA
[d] Manufacturing Engineering Department, Brigham Young University, Provo, UT 84602, USA

ARTICLE INFO

Keywords:
Microstructures
Dislocation density
Cyclic loading
Crystal plasticity
Aluminum alloys

ABSTRACT

The detailed contribution of microstructural-level phenomena, such as dislocation structure development and annihilation, as well as inter-granular and intra-granular backstress fields, to reverse loading behavior in metal alloys remains an area of active research and debate. The ability to predict unloading nonlinearities, the Bauschinger effect (BE), and changes in hardening rates during reverse loading is necessary for accurate modeling of deformation and springback in forming operations that involve strain path changes. This paper applies a recently developed elasto-plastic self-consistent (EPSC) crystal plasticity model to predict and interpret reverse loading in two commercially sensitive aluminum alloys (AA): 6016-T4 and 7021-T79. Model calibration and verification was enabled by an extensive experimental campaign of cyclic loading applied to the two alloys. The experimental data included hardening rates during monotonic tension, linear followed by non-linear unloading, the BE, and hardening rate changes during reverse loading that induce permanent softening. By considering anisotropic elasticity, dislocation density-based hardening, intra-granular slip system-level backstress fields, and inter-granular stress fields, the model predicted and quantified the contribution of different micro-scale phenomena to the observed behavior. The ability of the model to capture contrasting characteristics of the two alloys, particularly the distinct permanent softening and reloading yield stresses, demonstrated its ability to account for the co-dependent nature of crystallographic glide and the sources of hardening originating from the deformation history-dependent dislocation density evolution and backstress fields. Comparison of the experimental and modeling results revealed that the unloading behavior is primarily driven by backstress, the BE is governed by backstress and inter-granular stresses, and the hardening rates upon load reversals are controlled primarily by the strain-path sensitive evolution of dislocation density.

* Corresponding author: University of New Hampshire, Department of Mechanical Engineering, 33 Academic Way, Kingsbury Hall, W119, Durham, New Hampshire 03824, United States. Tel.: 603 862 5179; fax: 603 862 1865
E-mail address: marko.knezevic@unh.edu (M. Knezevic).

https://doi.org/10.1016/j.ijplas.2022.103292
Received 17 December 2021; Received in revised form 11 March 2022;
Available online 16 March 2022

1. Introduction

Accurate simulations of complex deformation processes are vital to the optimization of metal forming operations, along with the evaluation of component performance in service. Reliability of such simulations is dependent on a material model, which describes the relations between the imposed boundary conditions on a workpiece and the resulting deformation. As metal forming operations involve non-monotonic deformation paths with frequent unloading, the material model must be able to describe the material response under such deformation conditions. For example, bending-unbending of metallic sheets drawn over a die radius includes tension followed by compression (Chun et al., 2002; Knezevic et al., 2019; Poulin et al., 2020a; Poulin et al., 2019; Poulin et al., 2020b; Wagoner et al., 2013). Furthermore, the final unloading operation results in springback deformation, which always happens after removal of a part from a die (Barrett et al., 2020b; Boger et al., 2005; Wagoner et al., 2013). Predicting such behavior requires elasto-plastic material models able to predict unloading, transients in yield stress (the Bauschinger effect, BE), and changes in the work hardening rates during strain-path changes, in addition to anisotropic hardening rate during monotonic deformation. These phenomena originate from the evolution of the underlying microstructure, and are captured to different extents in various models.

A recent implicit formulation of the elasto-plastic self-consistent (EPSC) model incorporates the microstructure-level processes that contribute to the behavior of interest, integrating anisotropic elasticity, a dislocation-based hardening law, and a slip system backstress law (Zecevic and Knezevic, 2019). The initial study successfully benchmarked the model against a drawing operation in a single aluminum alloy. In the current work, the interplay between dislocation processes and backstress accumulation is analyzed in more detail via a combined experimental and modeling study of load reversal deformation in two contrasting, and commercially important, aluminum alloys: AA6016-T4 and AA7021-T79. Data from an ambitious campaign of mechanical testing on the sheet alloys is presented, and analyzed to determine load reversal deformation characteristics. The data is then used to calibrate and validate the model. To initialize the model, texture and grain structure were measured using electron backscattered diffraction (EBSD) for both alloys. The model parameters are calibrated for each alloy using part of the test data. Based on the performance of the model against the remaining data, the model is validated as a tool for predicting hardening rates during monotonic tension and compression, linear and then a non-linear unloading, the BE, and hardening rates during continuous straining in the opposite direction along with the permanent softening, as a function of loading history for both alloys. In particular, the roles of backstress, inter-granular stresses and the strain-path sensitive evolution of dislocation density are examined in the context of unloading behavior, the Bauschinger effect, and hardening rates following load reversal. Current understanding of the key microscale phenomena captured in the enhanced EPSC model are discussed in the following paragraphs.

During load reversal, unloading strains consist of an initial elastic response followed by a small nonlinear component owing to small-scale yielding, attributed to a dislocation relaxation phenomenon (Mompiou et al., 2012; Pavlina et al., 2015; Sritharan and Chandel, 1997; Wagoner et al., 2013; Yoshida et al., 2002; Zhou and LeSar, 2012). The small scale back-flow during unloading is a result of accumulated micro backstress fields arising from dislocation pile-ups at grain boundaries (Seeger, 1957; Weng, 1979) or non-deforming particles (Brown and Clarke, 1975; Tanaka and Mori, 1970). The back-flow is accommodated by some re-emission of the dislocations from the pile-ups (Mompiou et al., 2012; Sritharan and Chandel, 1997), while relaxing the micro backstress fields. Since the amount of plastic deformation before unloading influences the magnitude of non-linear unloading, accurate modeling of prior plastic deformation is essential to capture the non-linear unloading using a constitutive model.

The Bauschinger commonly refers to a lower yield stress observed during reverse loading, compared with the yield stress during reloading in the original direction (Bauschinger, 1886). The BE effect can occur in deformation of polycrystals from inter- and intra-granular sources (Nieh and Nix, 1986; Sauzay, 2008; Stout and Rollett, 1990) as well as in single crystals solely from intra-granular sources (Buckley and Entwistle, 1956; Demir and Raabe, 2010; Gough et al., 1927; Greetham and Honeycombe, 1960). The microstructural description of the BE is well documented in (Abel, 1987; Bate and Wilson, 1986a). In single crystals, hard dislocation walls due to high dislocation density separated by soft regions due to low dislocation density can induce intra-granular long-range internal stresses (LRIS) (Kassner et al., 2013; Mughrabi, 1983). Geometrically necessary dislocations maintain compatibility at the interface between such hetero-structured regions giving rise to hardening. During deformation the internal stresses develop in the opposite direction from the applied loading. Upon reloading in the opposite direction, these internal stresses combine with the loading and cause a drop in the yield.

In precipitation hardened alloys, such as Al alloys, precipitate obstacles to mobile dislocations cause the BE. Dislocations shear precipitates on the slip plane until the array of obstacles becomes closely spaced and sufficiently strong to inhibit the forward motion. After the applied stress is removed, the dislocations relax and re-equilibrate locally (Orowan, 1948). If the strain-path is reversed, the backward stress necessary to move the dislocations is lower than the forward stress because the array of obstacles on the same path has been overcome during the forward motion and is less dense than the array that arrested the dislocations during the forward motion (Orowan, 1959). Another distribution of precipitates will eventually arrest dislocations moving in the opposite direction but the BE has manifested itself before that. The anisotropy in resistance to dislocation glide between forward and reverse directions causes the BE. In the case of non-shearable precipitates, dislocations bow out and then form loops as they break through the obstacles. The loops exert a repulsive force on the dislocations of the same sign moving in the same direction but attractive force for the dislocations of the same sign moving in the opposite direction, which manifests itself as the BE. These second phase particles induce a composite effect, where the particles share the applied stress and thus reduce the amount of stress in the matrix. The matrix then flows at a larger applied stress than it would in the absence of the particles. This load sharing phenomena can serve as an additional source of backstress fields (Bate et al., 1981, 1982).

In polycrystalline materials, the BE effect has additional sources in inter-granular stress fields, where crystal lattice orientation results in a distribution of grain hardness, with respect to the loading direction. Inter-granular stress fields arise due to strain

Table 1
Chemical composition of AA6016-T4 and AA7021-T79 (wt%).

	Al	Si	Mg	Fe	Mn	Zn	Cu	Ti	Cr	Zr
AA-6016 T4	Balance	1.0-1.5	0.25-0.6	0.5	0.2	0.2	0.2	0.15	0.1	-
AA-7021-T79	Balance	0.25	1.2-1.8	0.4	0.1	5.0-6.0	0.25	0.1	0.05	0.08-0.18

incompatibilities between adjacent soft/hard grains during forward loading. These stress fields subsequently combine with the stress applied in the reverse direction, which can manifest in the drop of the yield stress (Weng, 1979, 1980). Importantly, these inter-granular stress fields are strongly linked to the evolutions of texture and grain structure with plastic strain, which promote the development of plastic anisotropy.

Following the BE, a change in the work hardening rate may occur (Hasegawa et al., 1975b; Jahedi et al., 2014; Kitayama et al., 2013a; Stout and Rollett, 1990; Wilson et al., 1990). As a result, an offset between the reverse and the forward flow stress arises (Bate and Wilson, 1986b; Orowan, 1959; Zang et al., 2013). The offset is referred to as permanent softening. The effect stems from a tradeoff between the annihilation of dislocations formed during the forward deformation and buildup of new dislocations during deformation in the opposite direction.

A range of macroscopic models have been formulated to predict cyclic deformation of alloys relying on a combination of isotropic and linear or nonlinear kinematic hardening laws (Armstrong and Frederick, 1966; Chaboche and Rousselier, 1983; Chaboche, 1977; Chaboche, 2008; Hu et al., 1992; Jahedi et al., 2015; McDowell, 1992; Ohno et al., 2021). These formulations are generally computationally efficient and suitable for easy implementation in finite element (FE) codes. These models mathematically represent the above mechanistic sources of backstress fields using a set of model parameters, but generally do not distinguish between intra- and inter-granular sources of backstress. Moreover, they employ a large number of adjustable parameters, which demand specialized mechanical tests and inverse methodologies for their identification (Feng et al., 2020; Smith et al., 2014). The models are also restricted to the specific material state used in testing and often to the specific loadings used during the model adjusting process.

Models based on crystal plasticity provide more flexibility to incorporate the mechanistic sources of backstress fields along with the crystallography of deformation mechanisms and texture. These models are not constrained to a specific deformation condition or a given material state and can predict the development of the anisotropy caused by the evolution of textural and microstructure (Barrett et al., 2019; Iftikhar et al., 2021; Knezevic and Beyerlein, 2018; Lopes et al., 1999). To link response of individual grains to the response of a polycrystalline aggregate, several homogenization schemes have been formulated. These range from upper-bound Taylor (Knezevic et al., 2009; Knezevic and Kalidindi, 2007; Knezevic et al., 2008a; Knezevic et al., 2008b; Taylor, 1938) to mean-field self-consistent (SC) (Feng et al., 2021; Lebensohn and Tomé, 1993; Riyad et al., 2021; Zecevic et al., 2018a; Zecevic et al., 2016b), and finally to spatial full-field formulations (Eghtesad et al., 2018a; Eghtesad et al., 2020; Eghtesad et al., 2018c; Feather et al., 2020; Feather et al., 2021; Kalidindi et al., 1992; Kalidindi et al., 2006; Knezevic et al., 2010; Lebensohn et al., 2012). While the full-field models are more accurate, by accounting for grain-to-grain interactions, the Taylor and SC models are computationally more efficient and effective in capturing the flow stress response and texture evolution. Additionally, Taylor and SC (including EPSC) models have been coupled with FE codes to relax the homogenization assumptions and incorporate spatially varying deformation (Ardeljan et al., 2016; Barrett and Knezevic, 2019; Barrett et al., 2020a; Feather et al., 2019; Knezevic et al., 2016; Knezevic et al., 2014; Knezevic et al., 2013b; Segurado et al., 2012; Zecevic et al., 2017a; Zecevic and Knezevic, 2017; Zecevic and Knezevic, 2018b; Zecevic and Knezevic, 2019; Zecevic et al., 2016a). The assumptions become relaxed because the deformation varies spatially from point to point across the FE mesh.

Details of incorporation of the various discussed contributing phenomena into a suitable EPSC model are discussed below, following a brief overview of the experimental test campaign.

2. Materials and experiments

Two precipitation-hardened alloys, commonly used for various lightweighting efforts in the automotive industry, were studied in sheet form: AA6016-T4 and AA7021-T79 (supplied by Commonwealth Rolled Products). The investigated AA6016-T4 was a 1.1 mm thick sheet, aged for about one year. It is a heat treatable low copper, Al–Si–Mg alloy in the temper T4 condition Table 1 shows its chemical composition. The Mg and Si content are set to produce Mg_2Si precipitates (Jaafar et al., 2012). The following precipitation sequence strengthens the alloy (Miao and Laughlin, 1999): supersaturated solid solution (sss) → Guinier–Preston (GP) zones → needle-like β'' → rod-like β' + lath-like precipitates → β + Si. These precipitate are barriers to dislocation motion, with the β'' phase proving the most effective for hardening (Eskin and Kharakterova, 2001). The investigated AA7021-T79 was a 2.5 mm thick sheet, also aged for about a year. The alloy was in T79 temper condition Table 1. shows its chemical composition. Heat treatment of this Al-Zn-Mg-Cu alloys result in a typical precipitation sequence as follows: sss → GP zones (coherent) → η' (metastable and semicoherent) → η ($MgZn_2$ – incoherent resulting from over-aging) (Couturier et al., 2017; Mirihanage et al., 2021; Prabhu, 2015). Unfortunately, the use of this alloy in industry is restricted by its low formability at room temperature. Warm forming greatly improves its formability with a possibility to form some precipitates dynamically. The alloy is being increasingly evaluated for various application as a part of an industry-wide lightweighting effort; AA6016-T4 has already been employed for components like exterior body panels, as it can be formed at room temperature. The AA6016-T4 is usually strengthened during the subsequent paint bake process (about 175°C for 20 minutes). The paint bake results in final properties that are stronger than T4, but not quite at the level of T6 condition. In addition to

high industrial relevance, these precipitation hardened alloys develop backstress fields and their effects on the load reversal behavior deserve to be systematically studied (Anjabin et al., 2014; Sehitoglu et al., 2005; Zecevic and Knezevic, 2015; Zecevic et al., 2016c).

Various experimental setups have been developed to test materials under strain path reversals, including forward - reverse torsion (Chen et al., 1999; Stout and Rollett, 1990), forward - reverse shear (Gracio et al., 2004), tension - torsion (Brown, 1970), tension - shear (Barlat et al., 2003; Peeters et al., 2001), and tension - compression (Boger et al., 2005; Dietrich and Turski, 1978; Szczepiński, 1990; Tan et al., 1994; Yoshida et al., 2002). In this work, the investigated alloys are tested monotonically in tension and compression and in single and multiple tension-compression cycles to various pre-strain levels. Specimens were cut out of the sheets with orientations along the rolling direction (RD) and the transverse direction (TD) according to the dimensions provided in appendix A. To verify that the tension portion of the cyclic curves matches data of regular tension tests, additional tensile bars were made according to the ASTM E-8 standard and tested on an MTS Landmark 370 servo-hydraulic testing machine. During these experiments, the strain was measured using the VIC-2D Digital Image Correlation (DIC) system. The load reversal experiments were performed on the testing setup developed in earlier works (Kuwabara et al., 2009; Kuwabara et al., 2001; Verma et al., 2011). The load cell used was TCLM -50KNB (Tokyo Sokki Kenkyujo Co., Max. load: 50 kN). The strain was measured using high-elongation strain-gages, YFLA-2-1L (Tokyo Measuring Instruments Laboratory Co.). A nominal strain rate of 10^{-4} /s was used for all tests. All tests were performed at room temperature.

3. Modeling framework

This section summarizes the EPSC polycrystal model used for modeling of the alloys. The particular version of the code is described in (Zecevic and Knezevic, 2019). The EPSC model treats a polycrystalline aggregate as a collection of ellipsoids/grains with a specific crystal lattice orientation and a volume fraction per orientation. Shape and crystallography of elipsoids evolve with plastic strain. Polycrystalline properties are obtained through the use of the SC homogenization scheme. In this scheme, each ellipsoid/grain is considered as an elasto-plastic inclusion embedded in the homogeneous-equivalent-medium (HEM). The HEM properties are the sought properties of the polycrystalline aggregate. In the model description below, we use "·" to denote a contracted/dot product and " $\otimes$ " notation to denote an outer/tensor product. Tensors are denoted by bold letters, while scalars are not bold.

The constitutive relation between Jaumann stress rate, $\widehat{\boldsymbol{\sigma}}$, and strain rate, $\dot{\boldsymbol{\varepsilon}}$, is used in EPSC at both a single crystal-level and at a polycrystalline aggregate-level (Nagtegaal and Veldpaus, 1984; Neil et al., 2010)

$$\widehat{\boldsymbol{\sigma}} = \mathbf{L}\dot{\varepsilon} = \dot{\boldsymbol{\sigma}} + \boldsymbol{\sigma}\mathbf{W} - \mathbf{W}\boldsymbol{\sigma} \tag{1}$$

At the polycrystalline level, the tensors, $\boldsymbol{\sigma}$, $\mathbf{W}$, and $\mathbf{L}$ are the Cauchy stress, spin, and tangent stiffness, respectively; such values at the single crystal-level are represented with a superscript, c as $\boldsymbol{\sigma}^c$, $\mathbf{W}^c$, and $\mathbf{L}^c$. Given the crystal quantities, the macroscopic Cauchy stress rate is obtained as $\dot{\boldsymbol{\sigma}} = \widehat{\boldsymbol{\sigma}} + \langle \mathbf{W}^c\boldsymbol{\sigma}^c\rangle - \langle \boldsymbol{\sigma}^c\mathbf{W}^c\rangle = \mathbf{L}\dot{\varepsilon} + \langle \mathbf{W}^c\boldsymbol{\sigma}^c\rangle - \langle \boldsymbol{\sigma}^c\mathbf{W}^c\rangle$, with $\mathbf{L}$ obtained using the standard iterative SC procedure (Eshelby, 1957; Lipinski and Berveiller, 1989; Turner and Tomé, 1994) from the volume averages $\widehat{\boldsymbol{\sigma}} = \langle \widehat{\boldsymbol{\sigma}}^c\rangle$ and $\dot{\boldsymbol{\varepsilon}} = \langle \dot{\boldsymbol{\varepsilon}}^c\rangle$. Hooke's constitutive law is used at the crystal-level

$$\widehat{\boldsymbol{\sigma}}^c = \mathbf{L}^c\dot{\boldsymbol{\varepsilon}}^c = \mathbf{C}^c\left(\dot{\boldsymbol{\varepsilon}}^c - \dot{\boldsymbol{\varepsilon}}^{pl,c}\right) - \boldsymbol{\sigma}^c tr(\dot{\boldsymbol{\varepsilon}}^c), \tag{2}$$

where $\mathbf{C}^c$ and $\dot{\boldsymbol{\varepsilon}}^{pl,c}$ are the elastic stiffness and the plastic strain rate tensors per crystal c, respectively. The plastic strain rate tensor is

$$\dot{\boldsymbol{\varepsilon}}^{pl,c} = \sum_s \mathbf{m}^s\dot{\gamma}^s \tag{3}$$

where $\mathbf{m}^s = \frac{1}{2}(\mathbf{b}^s \otimes \mathbf{n}^s + \mathbf{n}^s \otimes \mathbf{b}^s)$ is the symmetric Schmid tensor and $\dot{\gamma}^s$ is the shearing strain rate. The former is defined by the slip system geometry: $\mathbf{b}^s$ is the Burger's vector and $\mathbf{n}^s$ is the slip system plane normal. The index, s, enumerates available slip systems in every grain c. Slip system activation is based on the following two conditions

$$\mathbf{m}^s \cdot \boldsymbol{\sigma}^c - \tau^s_{bs} = \tau^s_c, \tag{4}$$

$$\mathbf{m}^s \cdot \widehat{\boldsymbol{\sigma}}^c - \dot{\tau}^s_{bs} = \dot{\tau}^s_c, \tag{5}$$

where, τ^s_c, is the resistance to slip and τ^s_{bs} is the slip system-level backstress determining the kinematic hardening effects (Wollmershauser et al., 2012). Condition 4 implies that the stress state is on the single crystal yield surface. Condition 5 ensures consistency that the stress state stays on the single crystal yield surface (Knockaert et al., 2000; Lentz et al., 2015; Zecevic et al., 2019). The quantities evolve using

$$\dot{\tau}^s_c = \sum_{s'} h^{ss'}\dot{\gamma}^{s'}, \tag{6}$$

$$\dot{\tau}^s_{bs} = \sum_{s'} h^{ss'}_{bs}\dot{\gamma}^{s'}, \tag{7}$$

where, $h^{ss'}$ and $h^{ss'}_{bs}$ are the hardening matrix consisting of derivatives, $h^{ss'} = \frac{\partial \tau^s_c}{\partial \gamma^{s'}}$, and the backstress matrix consisting of derivatives, $h^{ss'}_{bs}$

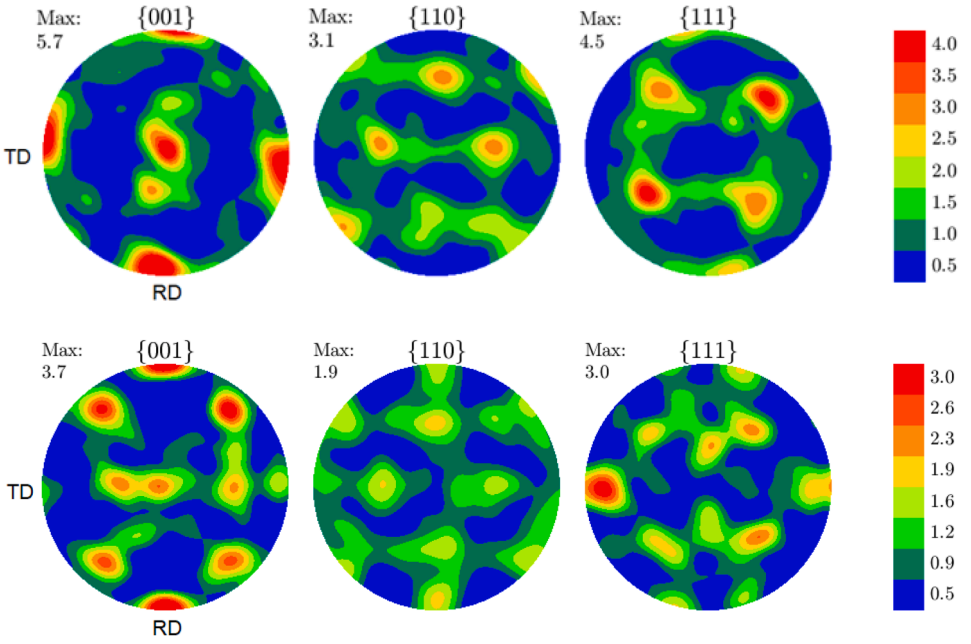

Fig. 1. Pole figures showing measured initial texture for AA6016-T4 temper 1.1 mm thick sheet aged for about one year (top) and AA7021-T79 temper 2.5 mm thick sheet also aged for about one year (bottom).

$= \frac{\partial \tau_{bs}^{s}}{\partial \gamma^{s}}$. The expressions for these derivatives are given in appendix B. Remaining to define at the single crystal level $\mathbf{L}^{c} = \mathbf{C}^{c} - \mathbf{C}^{c}\sum_{s}\mathbf{m}^{s} \otimes (\sum_{s'}(X^{ss'})^{-1}\mathbf{m}^{s'}(\mathbf{C}^{c} - \boldsymbol{\sigma}^{c} \otimes \mathbf{i})) - \boldsymbol{\sigma}^{c} \otimes \mathbf{i}$ with $X^{ss'} = h^{ss'} + h_{bs}^{ss'} + \mathbf{C}^{c} \cdot \mathbf{m}^{s} \otimes \mathbf{m}^{s'}$.

Finally, to calculate the reorientation of individual crystals with plastic strain, the lattice spin tensor, $\mathbf{W}^{c}$, is

$$\mathbf{W}^{c} = \mathbf{W}^{app} + \boldsymbol{\Pi}^{c} - \mathbf{W}^{p,c} \tag{8}$$

with $\mathbf{W}^{app}$ as the applied rotation rate, $\boldsymbol{\Pi}^{c}$ as the antisymmetric part of the Eshelby tensor (Lebensohn and Tomé, 1993), and $\mathbf{W}^{p,c}$ as the plastic spin, which is obtained from the shearing rates as

$$\mathbf{W}^{p,c} = \sum_{s} \mathbf{q}^{s} \dot{\gamma}^{s}, \tag{9}$$

with $\mathbf{q}^{s} = \frac{1}{2}(\mathbf{b}^{s} \otimes \mathbf{n}^{s} - \mathbf{n}^{s} \otimes \mathbf{b}^{s})$.

Next, we summarize the evolution laws for slip resistance and backstress to define the above partial derivatives. To this end, the EPSC model incorporates a strain-path sensitive hardening law based on dislocation density for the evolution of slip system resistance and a slip system-level backstress law to affect the activation resolved shear stress. These laws in combination with the latent hardening are aimed at predicting the anisotropic mechanical response of the alloys during monotonic tension/compression as well as the particularities pertaining to the load reversal deformation i.e. the nonlinear unloading, the BE, and changes in the hardening rates during load reversals. It should also be emphasized that since the model is elasto-plastic, the inter-granular stresses are obtained using the SC homogenization. Modeling anisotropic elasticity is essential in attempting to predict the response under non-monotonic loading and, especially, under unloading of pre-strained alloys because of the inter-granular stress fields.

In the formulations, $s+$ and $s-$ denote a positive and a negative slip direction on the given slip plane for every s belonging to a slip family/mode α. Resistance to slip involves three terms

$$\tau_{c}^{s} = \tau_{0} + \tau_{forest}^{s} + \tau_{debris}, \tag{10}$$

with τ_0 representing the friction Peierls stress, barrier strengthening, solid solution strengthening, and precipitation strengthening but otherwise dislocation free fixed value of slip resistance, while τ_{forest}^{s} and τ_{debris} are evolving terms with statistically stored forest and debris dislocation populations, respectively. These last two terms are

$$\tau_{forest}^{s} = b\chi G\sqrt{\sum_{s'} L^{ss'}\rho_{tot}^{s'}} \tag{11}$$

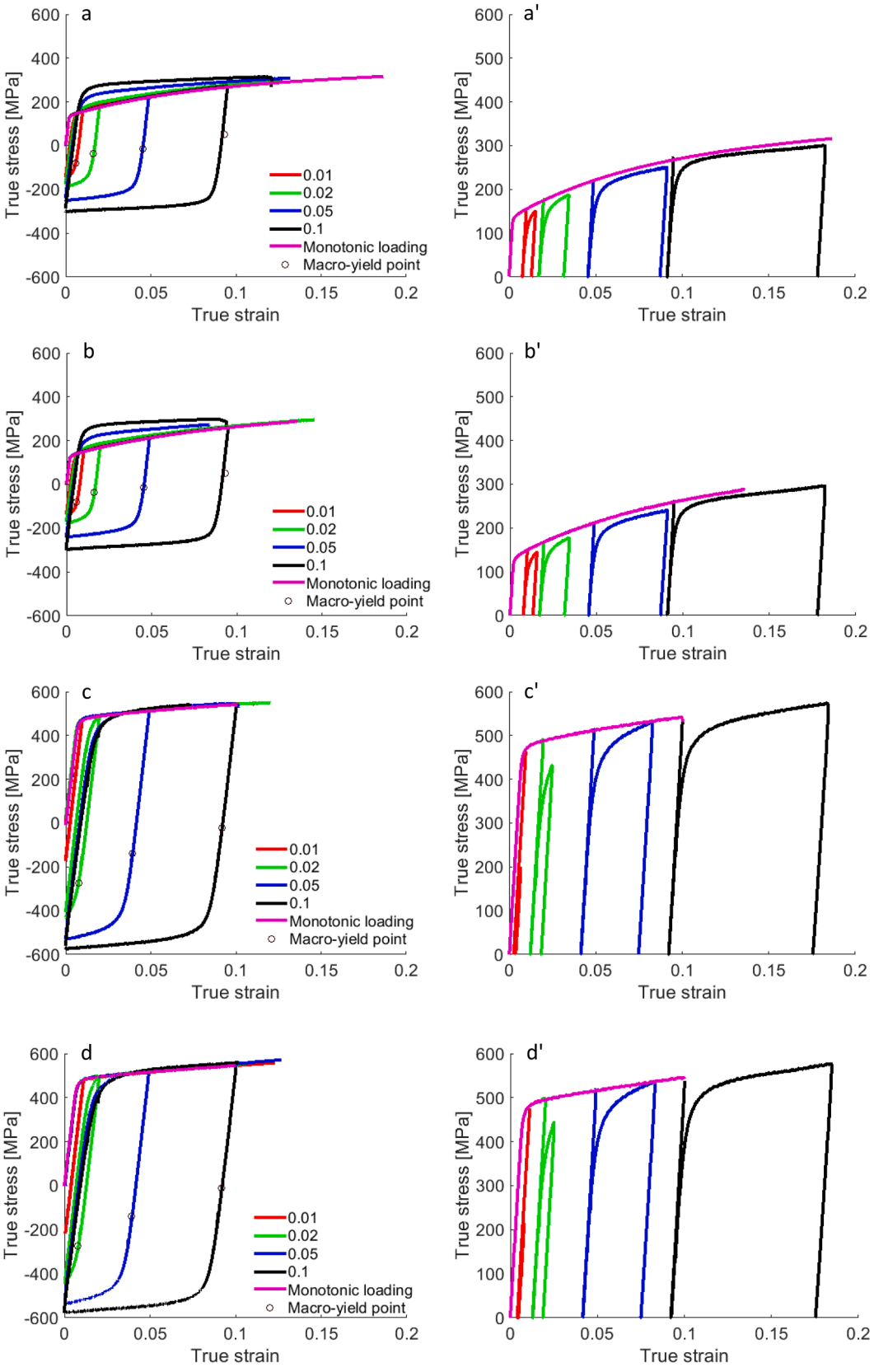

(caption on next page)

Fig. 2. True stress vs. true strain curves measured at room temperature during strain path reversals at four pre-strain levels in tension as indicated in the legends followed by compression to zero and then tension to fracture for AA6016-T4 along (a) RD and (b) TD and for AA7021-T79 along (c) RD and (d) TD. Macro-yield points during unloading and compression at 0.001 strain offset are indicated (σ_U). Comparison of monotonic loading in tension versus the 1st reversal (compression) curves as a function of accumulated true strain showing the permanent softening phenomenon for AA6016-T4 along (a') RD and (b') TD and for AA7021-T79 along (c') RD and (d') TD. Legends in the 'unprimend' plots apply to the corresponding 'primed' plots.

$$\tau_{debris} = 0.086Gb\sqrt{\rho_{deb}}log\left(\frac{1}{b\sqrt{\rho_{deb}}}\right) \tag{12}$$

Here, b is the Burgers vector ($b = 2.86\ 10^{-10}$ m for Al), χ is an interaction constant (Ghorbanpour et al., 2020; Lavrentev, 1980; Mecking and Kocks, 1981) ($\chi = 0.9$), ρ^s_{tot} is the total density of forest dislocations for the s^{th} slip system, ρ_{deb} is the density of debris dislocations, G (26 GPa) is the shear modulus, and $L^{ss'}$ is a latent hardening interaction matrix (Ghorbanpour et al., 2017; Zecevic and Knezevic, 2018a).

The total population of forest dislocations consists of

$$\rho^s_{tot} = \rho^s_{for} + \rho^{s^+}_{rev} + \rho^{s^-}_{rev}, \tag{13}$$

where ρ^s_{for} is the forward density, while $\rho^{s^+}_{rev}$ and $\rho^{s^-}_{rev}$ are the reversible densities associated with the s^+ and s^- slip system directions. These densities of dislocations evolve with shearing on slip systems (Ferreri et al., 2022; Kitayama et al., 2013b; Knezevic et al., 2013a; Zecevic and Knezevic, 2019; Zecevic et al., 2015)

(If $d\gamma^{s^+} > 0$)

$$\frac{\partial \rho^s_{for}}{\partial \gamma^s} = (1-p)k_1\sqrt{\sum_{s'} g^{ss'}\rho^{s'}_{tot}} - k_2(\dot{\varepsilon},T)\rho^s_{for}, \tag{14}$$

$$\frac{\partial \rho^{s^+}_{rev}}{\partial \gamma^s} = pk_1\sqrt{\sum_{s'} g^{ss'}\rho^{s'}_{tot}} - k_2(\dot{\varepsilon},T)\rho^{s^+}_{rev}, \tag{15}$$

$$\frac{\partial \rho^{s^-}_{rev}}{\partial \gamma^s} = -k_1\sqrt{\sum_{s'} g^{ss'}\rho^{s'}_{tot}}\left(\frac{\rho^{s^-}_{rev}}{\rho^s_0}\right)^m, \tag{16}$$

(If $d\gamma^{s^-} > 0$)

$$\frac{\partial \rho^s_{for}}{\partial \gamma^s} = (1-p)k_1\sqrt{\sum_{s'} g^{ss'}\rho^{s'}_{tot}} - k_2(\dot{\varepsilon},T)\rho^s_{for}, \tag{17}$$

$$\frac{\partial \rho^{s^+}_{rev}}{\partial \gamma^s} = -k_1\sqrt{\sum_{s'} g^{ss'}\rho^{s'}_{tot}}\left(\frac{\rho^{s^+}_{rev}}{\rho^s_0}\right)^m, \tag{18}$$

$$\frac{\partial \rho^{s^-}_{rev}}{\partial \gamma^s} = pk_1\sqrt{\sum_{s'} g^{ss'}\rho^{s'}_{tot}} - k_2(\dot{\varepsilon},T)\rho^{s^-}_{rev}, \tag{19}$$

with $\rho^s_{for}(\gamma^s = 0) = \rho^s_{initial}$, $\rho^{s^+}_{rev}(\gamma^s = 0) = 0$ and $\rho^{s^-}_{rev}(\gamma^s = 0) = 0$. In the above equations, k_1 is a fitting hardening parameter controlling the rate of dislocation density increase, while k_2 is calculated to represent a rate-sensitive term controlling recovery of dislocations (Beyerlein and Tomé, 2008), p is a reversibility parameter in the range from 0 to 1 (established to be 0.2 for Al alloys), $g^{ss'}$ is another interaction matrix populated with 1.0 (Khadyko et al., 2016; Kocks et al., 1991; Teodosiu and Raphanel, 1991), m is another parameter controlling the rate of dislocation recombinations (the value is set to 0.5 (Wen et al., 2015)), and ρ^s_0 is the total density of dislocations at the strain-path reversal on the system, s^{th} (Kitayama et al., 2013b).

The value of k_2 is calculated based on the following relation (Beyerlein and Tomé, 2008; Risse et al., 2017)

$$\frac{k_2}{k_1} = \frac{\chi b}{g}\left(1 - \frac{k_B T}{Db^3}ln\left(\frac{\dot{\varepsilon}}{\dot{\varepsilon}_0}\right)\right), \tag{20}$$

with the Boltzmann constant, k_B, a reference strain rate, $\dot{\varepsilon}_0 = 10^7$, drag stress, D, and an effective activation enthalpy, g. The debris density of dislocation is incremented based on

$$d\rho_{deb} = \sum_s qb\sqrt{\rho_{deb}}\ k_2\rho^s_{tot}|d\gamma^s|, \tag{21}$$

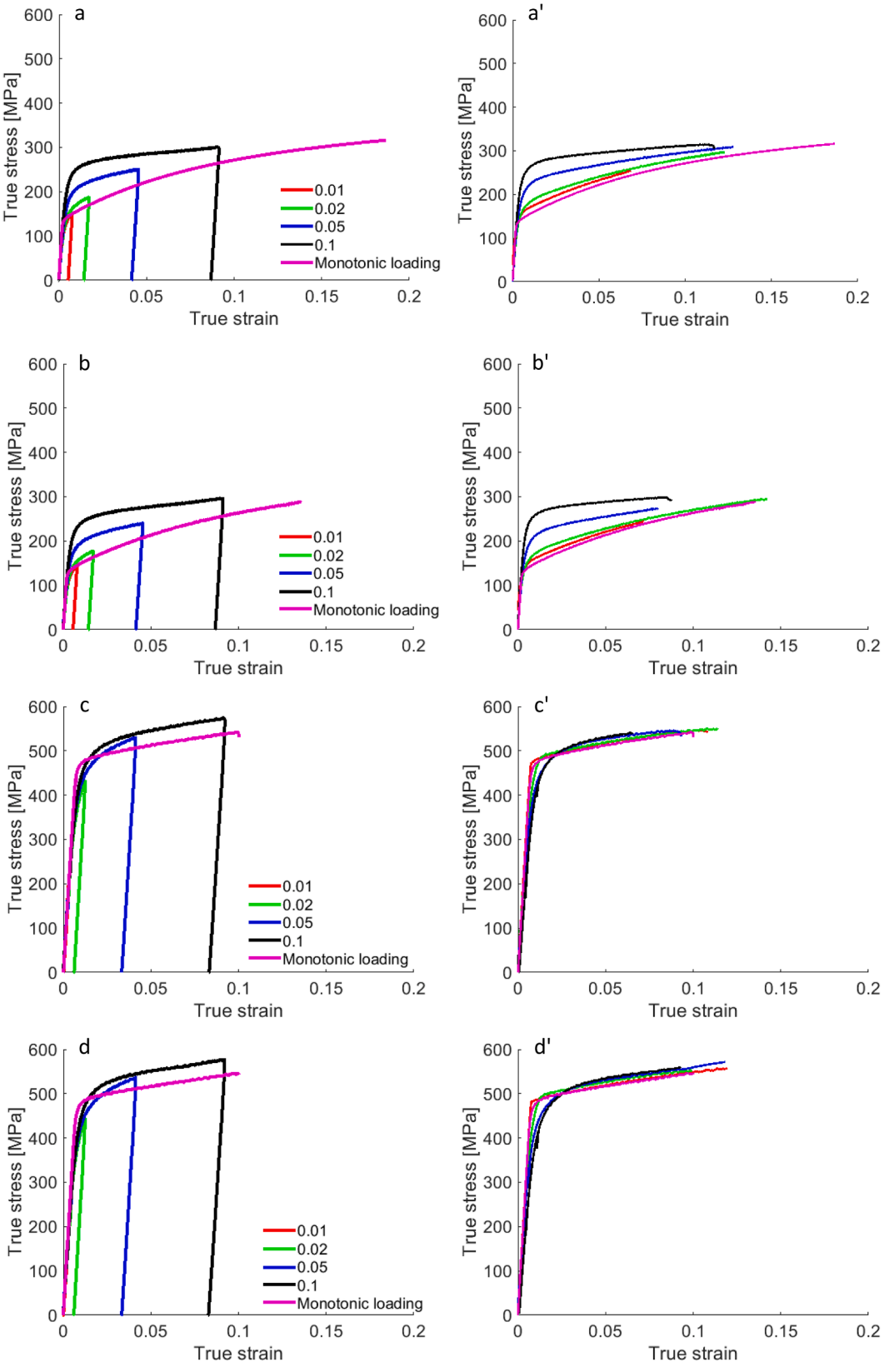

(caption on next page)

Fig. 3. Comparison of the monotonic loading in tension curves vs. the 1st reversal (i.e. compression) curves from Fig. 2 for AA6016-T4 along (a) RD and (b) TD and for AA7021-T79 along (c) RD and (d) TD. Comparison of the monotonic tension curves vs. the 2nd reversal (i.e. tension) curves from Fig. 2 for AA6016-T4 along (a') RD and (b') TD and for AA7021-T79 along (c') RD and (d') TD. Legends in the 'unprimend' plots apply to the corresponding 'primed' plots.

Table 2a
Fitting parameters for the evolution of slip resistance in AA6016-T4 and AA7021-T79.

	τ_0[MPa]	$k_1[m^{-1}]$	g	D[MPa]	$\rho^s_{initial}[m^{-2}]$
AA6016-T4	28	1.38×10^8	0.09	400	4.9e12
AA7021-T79	85	1.00×10^7	0.09	4000	1.5e14

with a fitting parameter q for the rate of dislocation recovery.

It remains to define a law for the evolution of backstress to calculate the backstress matrix, $h^{ss'}_{bs}$. Intra-granular sources of backstress are modeled by the phenomenological law as follows (Zecevic and Knezevic, 2019)

$$\tau^s_{bs} = \mathbf{m}^s \cdot \boldsymbol{\sigma}^c_{bs} = \tau^s_{bs,sys} + 2\sum_{s'} \mathbf{m}^s \cdot \mathbf{m}^{s'} \tau^{s'}_{bs,sys*}, \tag{22}$$

where

$$\tau^{s'}_{bs,sys*} = \begin{cases} \tau^{s'}_{bs,sys} \text{ if } \tau^{s'}_{bs,sys} > 0 \\ 0 \text{ if } \tau^{s'}_{bs,sys} < 0 \end{cases} \tag{23}$$

In the formulation, $\boldsymbol{\sigma}^c_{bs}$ is the backstress tensor based on the contribution from the slip system-level sources over s' when $s' \neq s$. The slip system-level sources are modeled using

(if $d\gamma^{s^+} > 0$ and $\tau^{s^+}_{bs,sys} > 0$)

$$\tau^{s^+}_{bs,sys} = \tau^{sat}_{bs}(1 - \exp(-\nu\gamma^{s^+})), \tag{24}$$

$$\tau^{s^-}_{bs,sys} = -A\tau^{s^+}_{bs,sys}, \tag{25}$$

(if $d\gamma^{s^+} > 0$ and $\tau^{s^+}_{bs,sys} < 0$)

$$\tau^{s^+}_{bs,sys} = -(A+1)\tau^{sat}_{bs}\exp\left(-\frac{\gamma^{s^-}}{\gamma_b}\right) + \tau^{sat}_{bs}, \tag{26}$$

$$\tau^{s^-}_{bs,sys} = -\frac{1}{A}\tau^{s^+}_{bs,sys}. \tag{27}$$

The law involves a saturation value, τ^{sat}_{bs}, a parameter governing an asymmetric evolution in $s+$ and $s-$, A, the denominator, γ_b, and a multiplier, ν, as fitting constants. The shearing strain, γ^s, is a value at the local load reversal. Important to note is that $\tau^{s^+}_{bs}$ opposes the driving force in s^+: $\mathbf{m}^{s+} \cdot \boldsymbol{\sigma}^c - \tau^{s+}_{bs} = \tau^s_c$, implying that $\tau^{s^+}_{bs}$ reduces the driving force. However, $\tau^{s^-}_{bs}$ aids the driving force in s^-: $\mathbf{m}^{c,s-} \cdot \boldsymbol{\sigma}^c - \tau^{s^-}_{bs} = \tau^s_c$.

4. Results

This section presents the experimental results first including texture and flow stress curves and then modeling results including calibration and verification.

4.1. Experimental

Fig. 1 shows pole figures depicting texture in the alloys, while inverse orientation maps collected using EBSD depicting grain structure are provided in appendix A. Texture is based on multiple EBSD scans. As expected, a cube texture component is predominant in the pole figures.

Table 2b
Fitting parameters for the evolution of back-stress in AA6016-T4 and AA7021-T79.

τ^s_{bs} [MPa]	ν	γ_b	A
12	560	0.001	1

Table 2c
Latent hardening parameters established in (Devincre et al., 2006; Hoc et al., 2004) for FCC metals.

a_0	a_1	a_2	a_3	a_4	a_5
0.068	0.068	0.0454	0.625	0.137	0.122

Fig. 2 shows measured true stress versus logarithmic strain curves recorded during tension-compression-tension strain path reversals. The first loading is monotonic tension to a given pre-strain level. The second strain-path is compression to zero strain (1st reversal). The third strain-path is tension to fracture or to a detachment of the strain gauge (2nd reversal). The materials exhibit typical decreasing work hardening rate during the monotonic tension, which is normal for plasticity facilitated by crystallographic slip. Upon the 1st reversal, the alloys exhibit a linear followed by a nonlinear portion of unloading. Macro yield points during unloading are

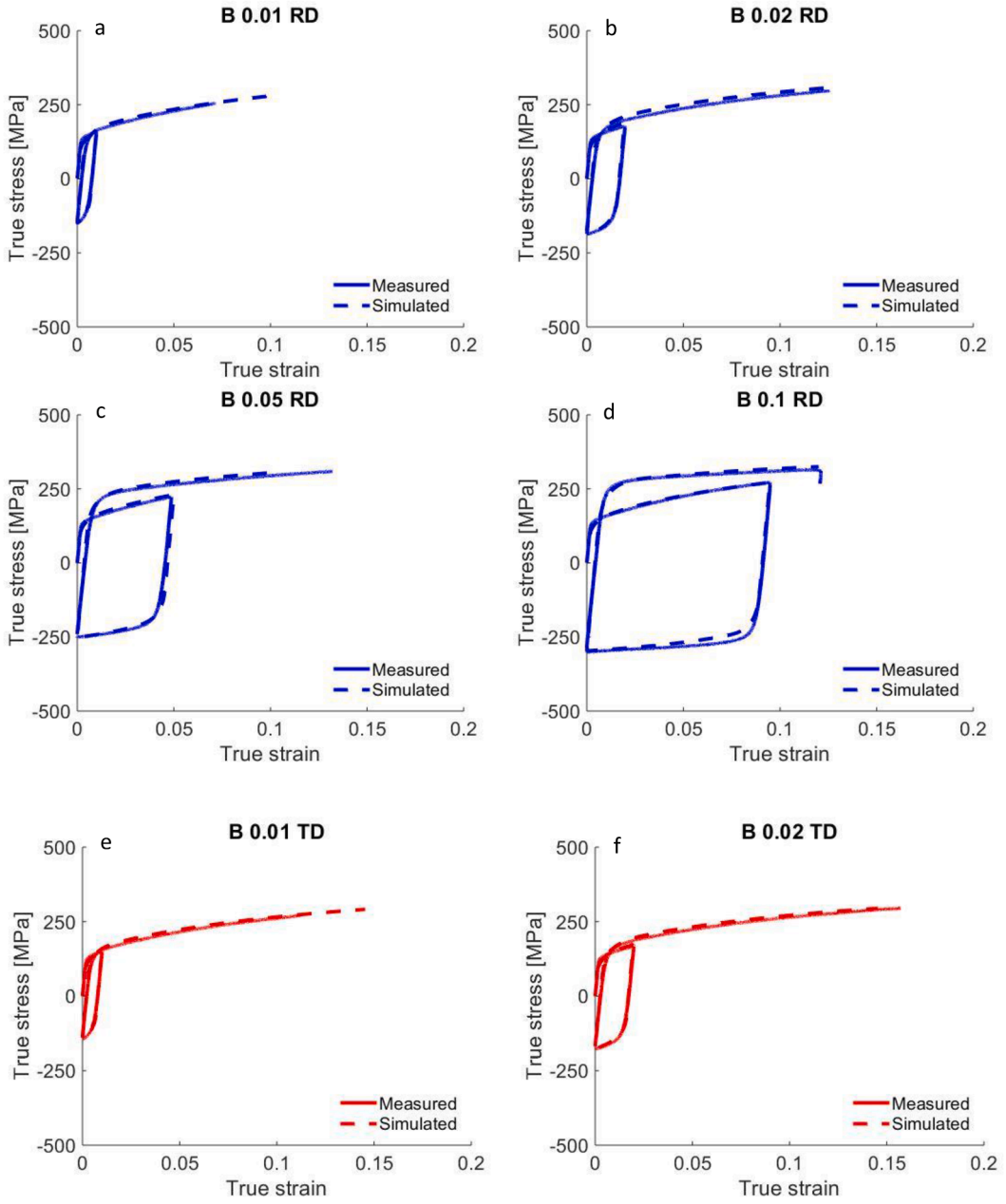

Fig. 4. Comparison of simulated and measured true stress-true strain response in strain path reversal deformation for AA6016-T4 along (a - d) RD and (e - h) TD and for AA7021-T79 along (i - l) RD and (m – p) TD.

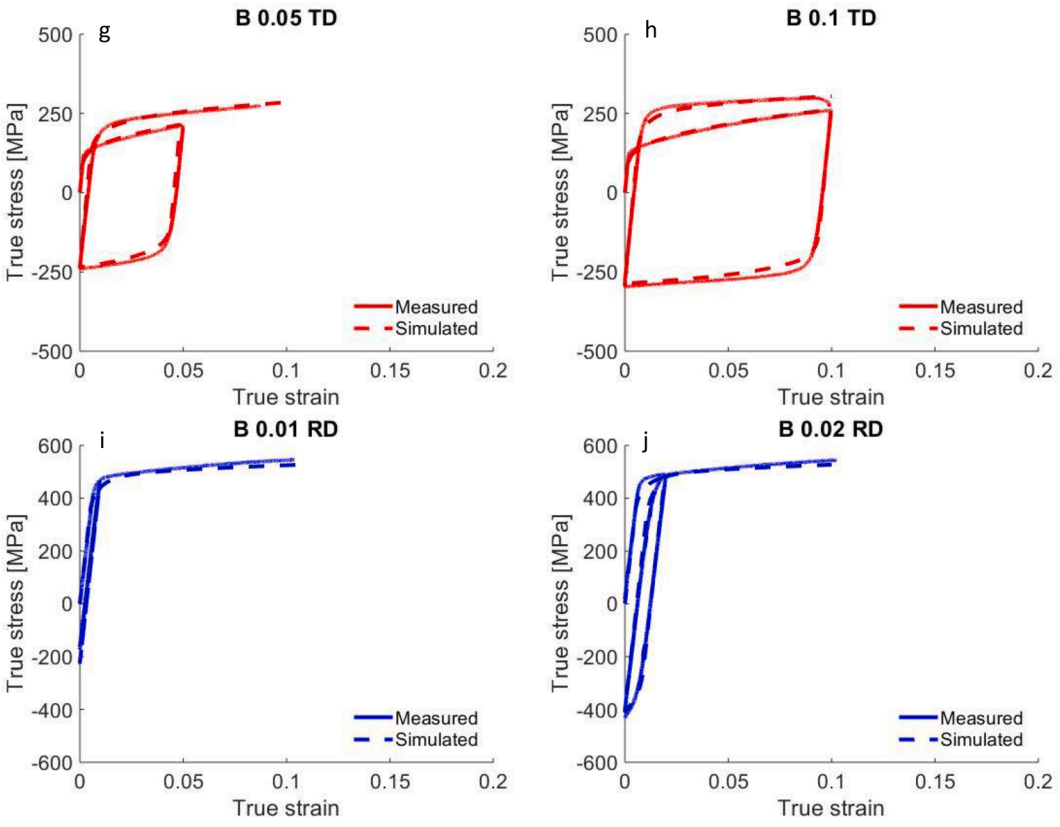

Fig. 4. (*continued*).

identified (σ_U) at approximately 0.001 offset. The level of pre-strain increases the magnitude of macro yield stress but decreases the extent of the linear unloading. The extent of linear and also nonlinear unloading is greater for the stronger alloy. The reduction of the yield stress achieved during the monotonic pre-straining to that during reverse straining is the BE or transient softening. Essentially, the resistance to dislocation glide in the reverse sense is less than in the forward sense. Like nonlinear unloading, the BE is enhanced with strength. After the transient softening comes the permanent softening. The phenomenon is depicted in the primed figures of Fig. 2. However, it is prominent only for the softer alloy. There is no lowering of the flow curves when the reverse stress-strain curves are plotted in the same direction as during the prior straining for AA7021-T79.

Fig. 3 shows comparisons between the monotonic tension and the 1st and 2nd reversals to observe the yielding differentials and successive hardening rates for the alloys. While transients after the 1st reversal and after the 2nd reversal are similar for AA6016-T4, they are smaller after the 2nd reversal for AA7021-T79. As the elasto-plastic transition upon the reversals (1st and the 2nd) is prolonged for both alloys, the strain hardening rates are reduced compared to those during the forward tension for AA6016-T4 but not for AA7021-T79. Interestingly, the strain hardening in compression substantially surpasses that of tension causing positive yield differentials for AA6016-T4. Such positive yield differential increases with pre-strain. However, the yield differential is much smaller for AA7021-T79. Upon macroscopic re-yielding, the rates of strain hardening are restored for both alloys. The yield differential behavior after the 2nd reversal is similar to that after the 1st reversal for AA6016-T4 but even smaller for AA7021-T79. The origin of these phenomena will be described and discussed later.

4.2. Modeling

This section presents the results of model calibration and verification using the data. The uniaxial deformation processes are simulated by applying increments in strain along the loading direction (RD or TD), while enforcing the normal stresses in the lateral directions as well as the shear strains to zero. The simulations are initialized with the measured texture per alloy.

The hardening law along with the backstress law fitting parameters were adjusted using one cyclic tension-compression-tension curve per alloy, as each fitting parameter affects a different portion of the fitted curve. The curve deformed to a monotonic tensile pre-strain of 0.05 was used in fitting. The identified parameters were fine-tuned using another cyclic curve per alloy. The remaining cyclic curves can be regarded as predictions. The parameters identified per alloy are the initial resistance to slip, τ_0^α, trapping rate coefficient, k_1^α, drag stress, D^α and activation barrier for de-pinning, g^α (Barrett et al., 2019; Eghtesad et al., 2018b; Knezevic and Landry, 2015; Savage et al., 2021). The identification procedure started by varying τ_0^α to reproduce onset in yielding. Next, k_1^α, was

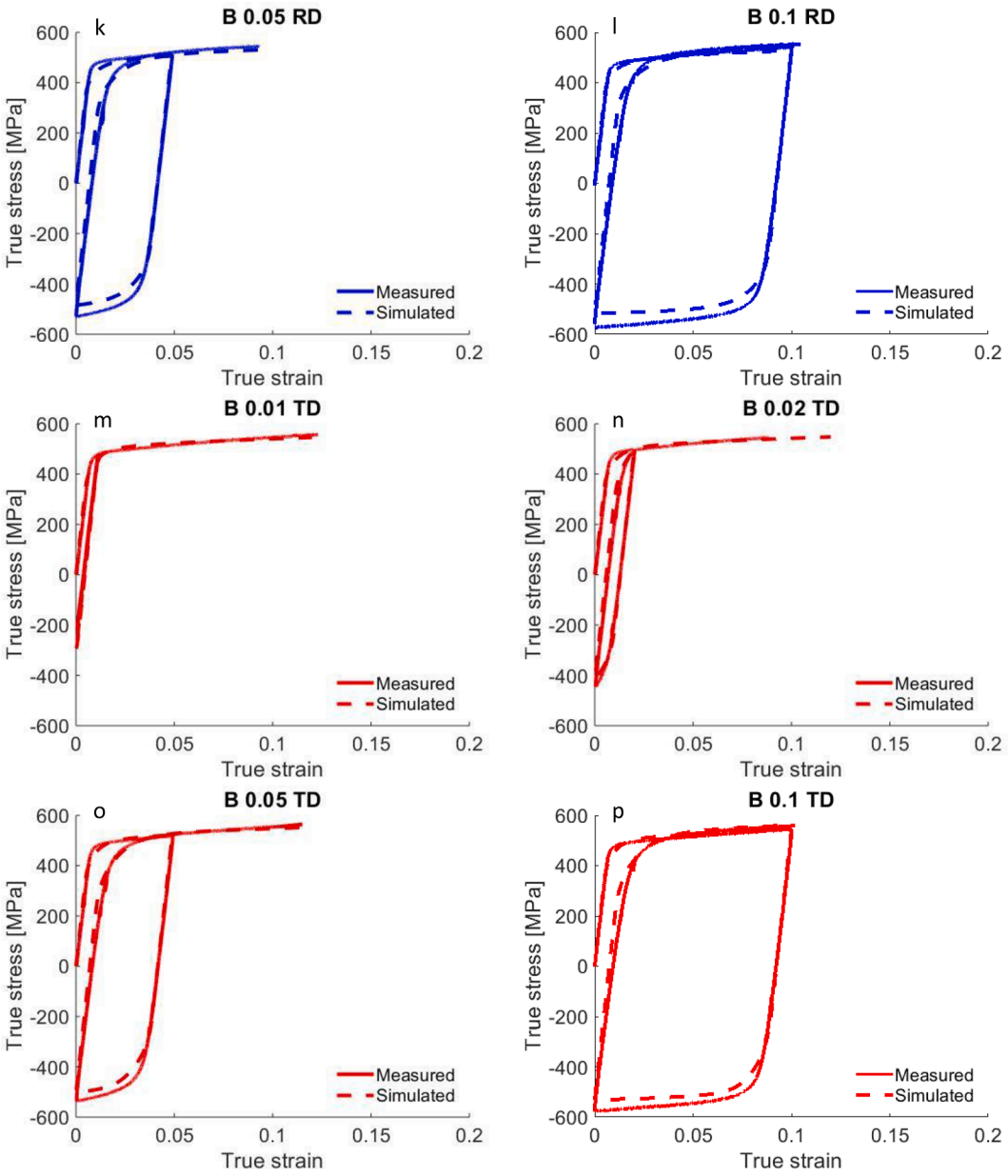

Fig. 4. (*continued*).

varied such that the initial hardening slopes are captured. Next, g^{α} and D^{α} are varied to match the latter hardening rates. Finally, q^{α} was fit to capture the later stage in the hardening rates. Concurrently with the hardening parameters, the backstress law parameters were identified. These included the saturation value for backstress τ_{bs}^{sat}, asymmetry factor, A, and coefficients ν and γ_b. τ_{bs}^{sat} and A were varied to obtain the unloading and yield at load reversals. Once these were achieved, tuning ν and γ_b simply provides better fits. The established parameters per alloy are given in Table 2a, Table 2b, and Table 2c.

Fig. 4 shows the comparison of measured and simulated tension-compression-tension curves for the alloys. These multiple-range hysteresis curves are modeled with good accuracy. In particular, the model reproduced the features specific to the load reversal behavior of the alloys including the hardening rates, nonlinear unloading, BE, and permanent softening. Next, the monotonic tension and compression curves were simulated Fig. 5. shows the comparison for the monotonic data. The simulated curves are predictions. Importantly, the small anisotropy due to texture and underlying deformation mechanisms and their anisotropic hardening including the latent hardening is captured. AA6016-T4 does not exhibit any asymmetry, which is also well predicted by the model.

Appendix A presents maps measured by EBSD over large areas for alloy AA6016-T4 after simple tension to a strain of 0.2 along RD and to a strain of 0.16 along TD. The development of misorientation spreads in individual grains as a consequence of plastic straining is

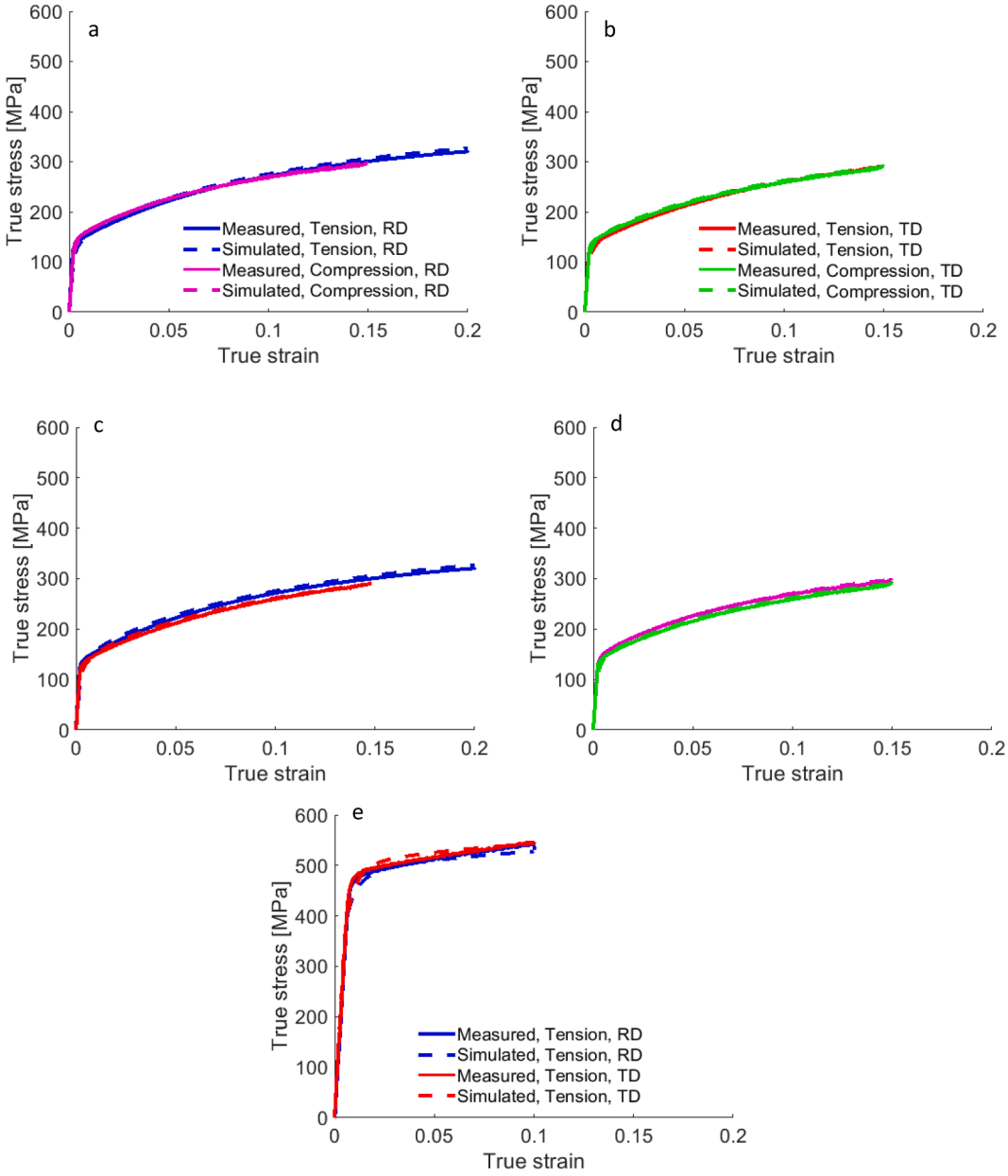

Fig. 5. Comparison of predicted and measured true stress-true strain response in monotonic (a – d) simple tension and compression for AA6016-T4 and (e) simple tension for AA7021-T79.

evident, especially in the RD direction because of the larger accumulated strain. The appendix also presents corresponding pole figures showing texture evolution in the alloy after simple tension. To verify the EPSC predictions, the texture data is compared with the model predictions. Since the plastic strain levels are relatively small, the texture evolution is not substantial. Nevertheless the model successfully reproduces the intensity levels and reorientation trends such as slight alignment of {111} pole with the loading direction, as expected for FCC metals (Kocks et al., 1998). Since the deformation strain levels for alloy AA7021-T79 are smaller than for AA6016-T4, the microstructure evolution in alloy AA7021-T79 is expected to be even less appreciable and is not presented.

Finally, the model is validated by simulating variable strain range and mean strain cycles for the alloys. The model was capable of capturing these complex data sets, also with good accuracy, as shown in Fig. 6. Although the model captures the yield point in the first cycle, re-yielding in the subsequent cycles is sometimes underpredicted in compression and overpredicted in tension. Moreover, the 2^{nd} unloading is overpredicted for the stronger alloy (Figs. 4k, l, o, p). Model modifications such as accounting for spreads in the field variables over ellipsoids could improve these predictions. In the present model, a single value is assumed for a given field across the entire ellipsoid. Such spreads have been incorporated in a visco-plastic SC (VPSC) formulation (Lebensohn et al., 2016; Zecevic et al.,

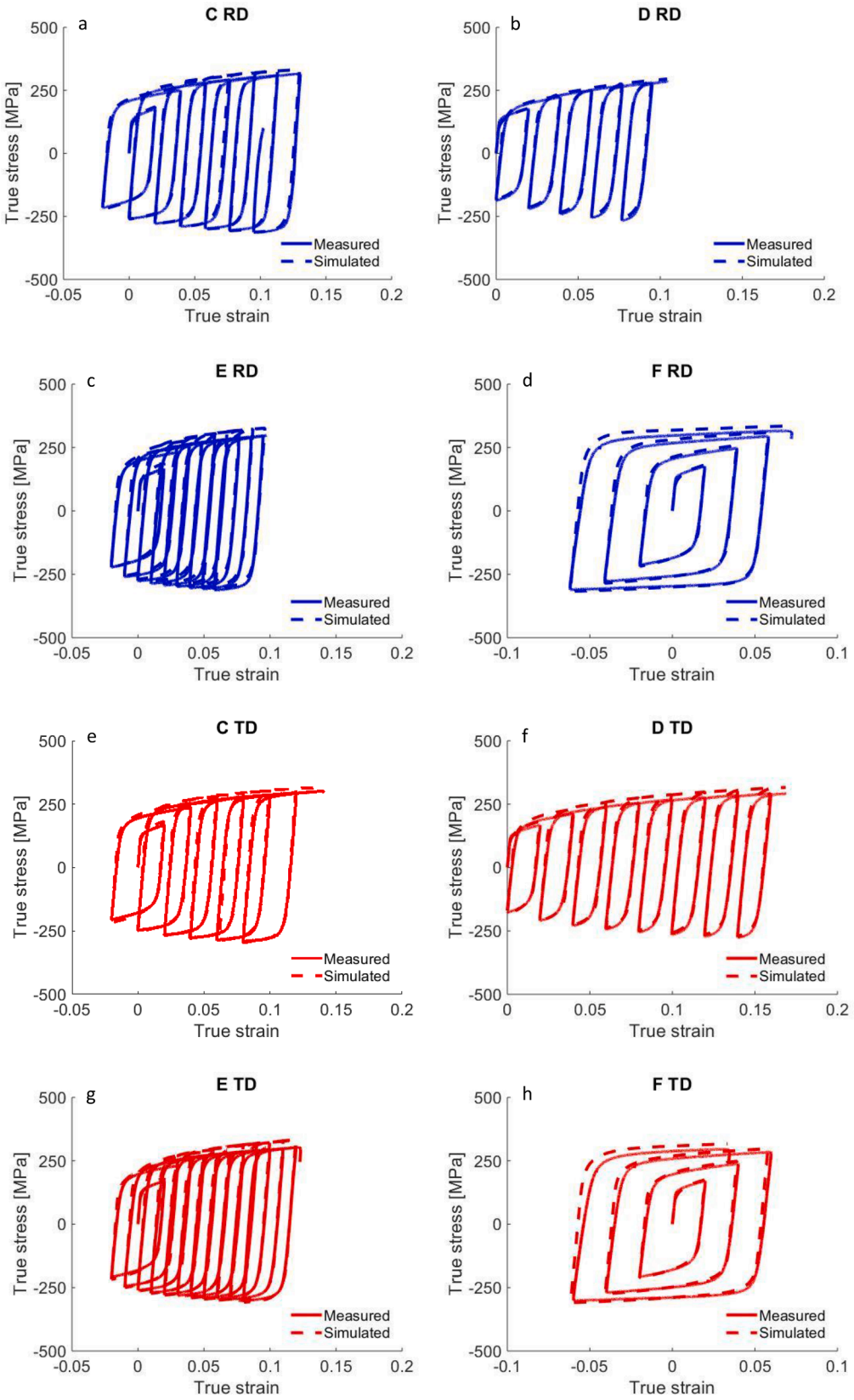
a
C RD
b
D RD
c
E RD
d
F RD
e
C TD
f
D TD
g
E TD
h
F TD
True stress [MPa]
True strain
Measured
Simulated

Fig. 6. Comparison of predicted and measured true stress-true strain response during multiple strain cycles for AA6016-T4 along (a - d) RD and (e - h) TD anf for AA7021-T79 along (i - l) RD and (m – p) TD. The strain path in (a, e, i, and m) is: 0 → 0.02 → -0.02 → 0.04 → 0 → 0.06…up to fracture with the strain range/amplitude of 0.04 and mean strain increment of 0.02 per cycle. The strain path in (b, f, j, and n) is: 0 → 0.02 → 0 → 0.04 → 0.02 → 0.06…up to fracture with the strain range/amplitude of 0.02 and mean strain increment of 0.02 per cycle. The strain path in (c, g, k, and o) is: 0 → 0.02 → -0.02 → 0.03 → -0.01 → 0.04…up to fracture with the strain range/amplitude of 0.04 and mean strain increment of 0.01 per cycle. The strain path in (d, h, l, and p) is: 0 → 0.02 → -0.02 → 0.04 → -0.04 → 0.06…up to fracture.

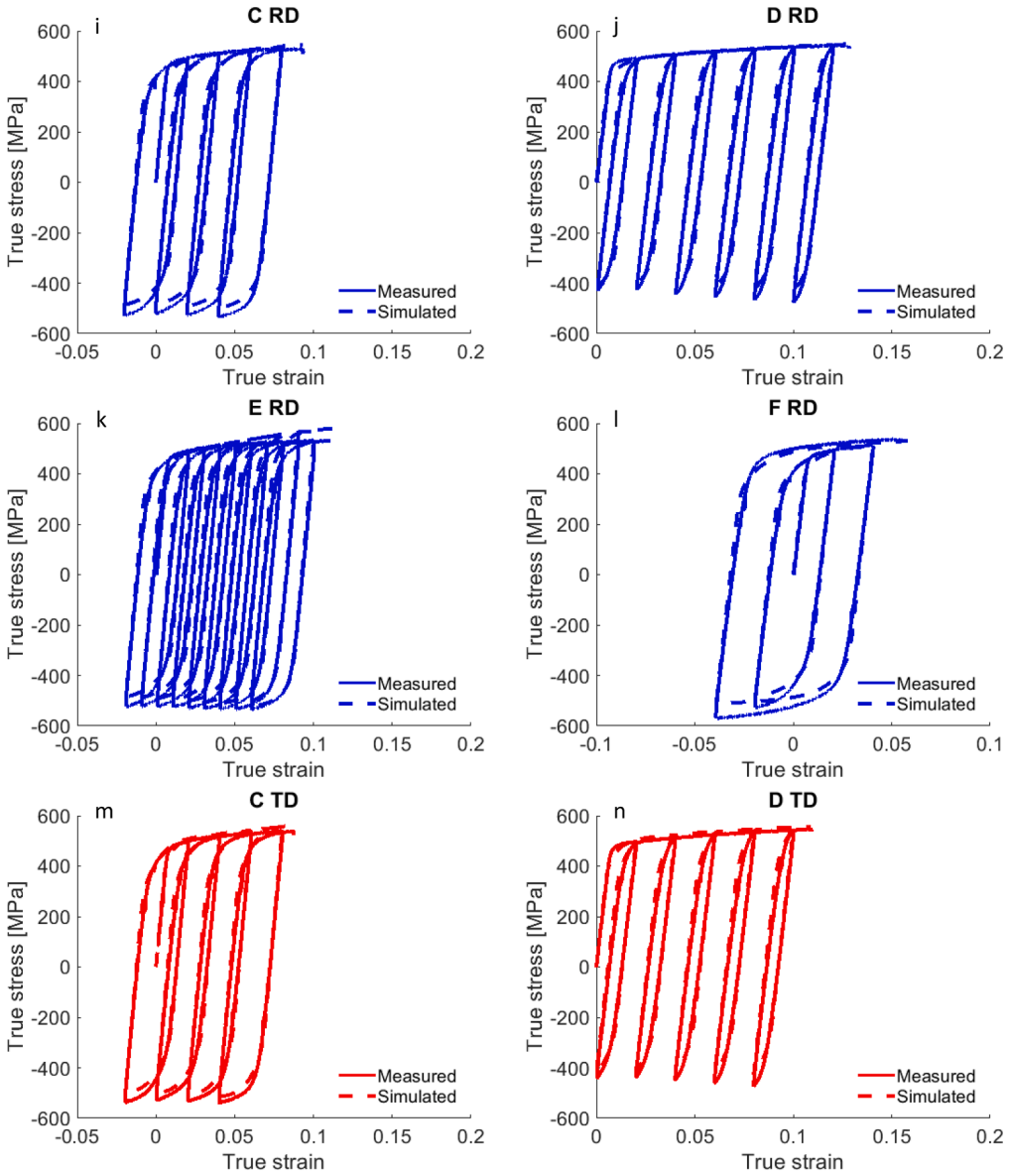

Fig. 6. (*continued*).

2020; Zecevic et al., 2018b; Zecevic et al., 2017b).

5. Discussion

This work reports comprehensive monotonic and load reversal data for two Al alloys and is concerned with predicting and interpreting the data using crystal plasticity modeling, which captures microstructural evolution and the directionality of crystal-level deformation mechanisms. The model is the EPSC formulation (Zecevic and Knezevic, 2019), which incorporates a dislocation density-based hardening law originally developed in (Beyerlein and Tomé, 2008) and later advanced to account for dissolution of dislocations upon load reversal and slip system-level backstress fields.

The data showed typical decreasing hardening rates with minor anisotropy RD versus TD, a linear and then a nonlinear unloading,

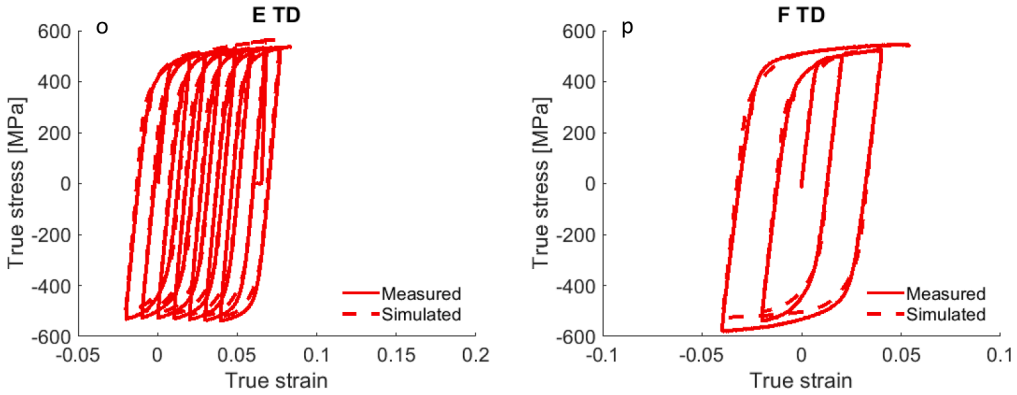

Fig. 6. (*continued*).

and the BE for both alloys. The data were employed to calibrate and validate the EPSC model. The performance of the model in capturing the complex deformation characteristics of the alloys is a consequence of accounting for kinematic hardening through the evolution law for backstress at the slip system-level, inter-granular stress fields, and annihilation to reproduce the stagnation or slight decrease in dislocation density upon strain-path reversal. Additionally, the model is initialized with the experimentally measured texture data and average grain shape for each grain per alloys. The aim is to provide physical insights into various aspects of the material response during strain-path reversals from the comparisons between data and predictions for both alloys.

To begin, we consider several additional parameters defined by looking at the overlap between the hysteresis loops and the monotonic tensile curves. The parameters are the reloading stress differential, $\Delta\sigma_h$, ratcheting strain, ϵ_Δ, and reloading softening stress, $\Delta\sigma_s$ Fig. 7.a illustrates these additional parameters. Additionally, the unloading deviation stress $\Delta\sigma$ is also quantified. The reloading yield stress differential under tension i.e. the differential between initial yield stress in tension and 2nd reversal yield stress is shown in Figs. 7b and c as a function of the applied tensile pre-strain. The differential increases with plastic strain for AA6016-T4, while it is nearly zero for AA7021-T79. Evidently, the increase in strength weakens the reloading yield effect, which is attributed to the difference in hardening rates i.e. primarily to a higher dislocation density (Table 2), and a slower buildup of dislocations with plastic strain in AA7021-T79 than AA6016-T4. Based on the data from Figs. 6a, b, e, f, i, j, m and n, the reloading softening stress is nearly zero for both alloys. As a result, the corresponding ratcheting strain is also negligibly small. These results are in contrast to recently reported results for dual phase steel sheets (Barrett and Knezevic, 2020). Finally, the unloading deviation stress is shown in Figs. 7d and e as a function of the applied pre-strain in tension. The deviation shows a decreasing trend with pre-strain, especially for the stronger alloy.

We regard the model as capable of predicting all of the phenomena associated with load reversal deformation of the alloys using a single set of parameters per alloy. The model predicts the cyclic behavior as a function of the loading direction and the level of pre-strain. With the model, we attempt to explain the deformation characteristics and underlying phenomena in the alloys during such deformation. Local stress in every grain is a consequence of the applied stress, inter-granular backstress fields, and intra-granular backstress fields. The model reveals that the backstress controls the nonlinear unloading deformation, early yielding upon reloading and immediate hardening that follows Fig. 8. shows the buildup of backstress with the accumulated shearing strain in a randomly selected grain per alloys for a slip system with the highest activity in the chosen grain. In a study done on steels in (Wilson and Bate, 1986), backstress was estimated using an X-ray diffraction technique. Results of measurements showed that backstress increased rapidly to 0.03 strain. After the strain-path reversal, the backstress quickly decayed to zero by 0.02 reverse strain. Our model predicts similar trends. Given that the unloading of both alloys is predicted using the same backstress parameters, the analysis shows that similar level of backstress fields develops in both alloys.

However, the intra-granular backstress and inter-granular stress fields are not sufficient to describe the flow stress upon strain-path reversals, as noted in (Orowan, 1948). Essentially, the reverse deformation would exhibit exactly the same shape of the flow curve as the original, just shifted along the stress axis. Subsequent deformation is controlled by the backstress and intergranular stress fields initially and then by the evolution of dislocation density. The annihilation of dislocation density upon strain-path reversal is an additional mechanism necessary for the accurate predictions of stress levels during strain-path reversal deformation. The effect is detected from a shrinkage in the diffraction peak widths upon strain-path reversal (Wilson and Bate, 1986). At the strain-path reversal, generation of dislocations is retarded momentarily because a fraction of loosely-tangled dislocations easily glides in the reverse direction (Beyerlein, 2008). Moreover, the stress relaxation takes place while the piled-up dislocations rearrange themselves into an equilibrium position with some annihilation of mobile dislocations.

Fig. 9 shows that the dislocation density evolution driven hardening rates are approximately 3x lower in AA7021-T79 than in AA6016-T4. The figure shows the volume average dislocation density evolution during the cyclic deformation for the alloys. Without the consideration of the reversible dislocations, the model would be able to predict the hardening rates after reversal. While the plots

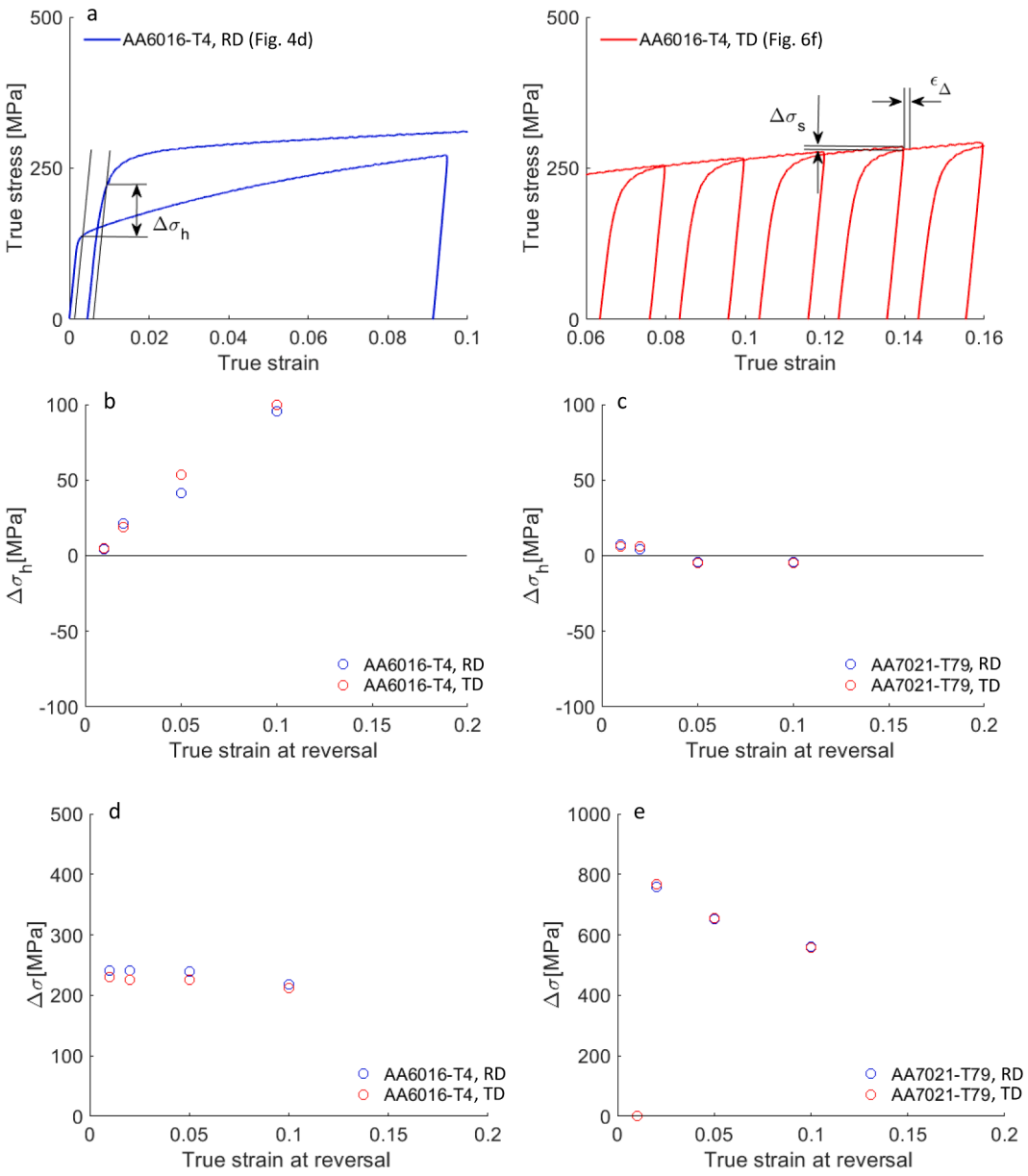

Fig. 7. (a) Schematics defining the reloading yield stress differential under tension ($\Delta\sigma_h$), ratcheting strain (ϵ_Δ), and reloading softening stress ($\Delta\sigma_s$). Comparison of $\Delta\sigma_h$ versus true strain levels for 1st reversal for (b) AA6016-T4 and (c) AA7021-T79. Unloading deviation stress ($\Delta\sigma = \sigma_L - \sigma_U$), where σ_L is the true stress at the end of a pre-load and σ_U is the macro-yield stress during unload at approximately 0.001 offset, for (d) AA6016-T4 and (e) AA7021-T79.

look similar for both alloys, substantially slower buildup of dislocation density is seen for AA7021-T79. Interestingly, some deformation can be accommodated without a marked increase in dislocation density. These predicted trends are in good agreement with the constitutive assumptions invoked in developing cyclic plasticity models in (Ohno, 1982; Ohno and Kachi, 1986). The easy motion and annihilation of reversible dislocations in the opposite direction is controlled by the reversibility parameter. The effect of local reversible dislocation population for the reversibility parameter of 0.2 is shown in Fig. 10 for a grain in both alloys. Such evolution is typical for all grains with the accumulated shear strain on a slip system mediating the issue of over-predicting of the hardening upon the strain-path reversal. As result, the evolution of slip resistance is directional at the slip system level and evolves with these microstructure rearrangements upon load reversal Fig. 9. is a collective result for total dislocation density of all grains per alloy. The evolution of dislocation density is responsible for predicting the magnitude of permanent softening per alloy. The phenomenon was first described in (Hasegawa et al., 1975a) during tension-compression loading. It was also described for forward-reverse simple shear loading in (Gracio et al., 2004).

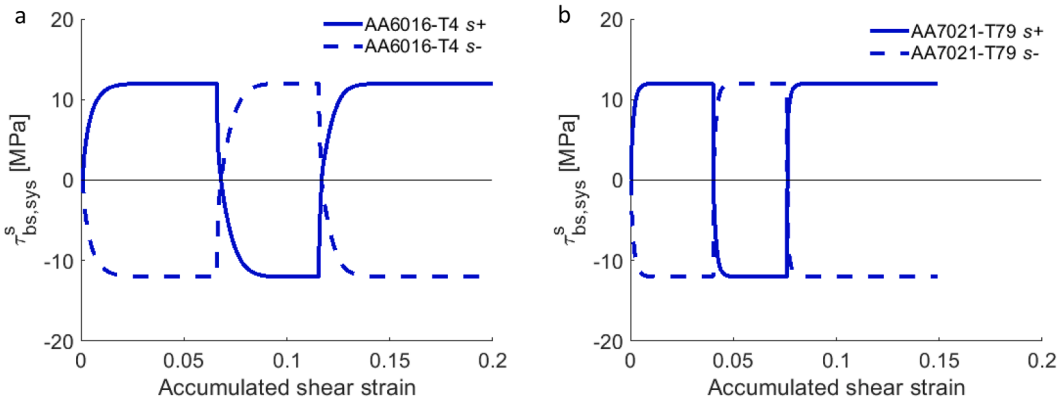

Fig. 8. Backstress vs. accumulated shear strain for an s^{th} slip system with the highest activity in a randomly selected grain during forward tension to 0.05 strain followed by the 1st and the 2nd reversal along RD for (a) AA6016-T4 and (b) AA7021-T79.

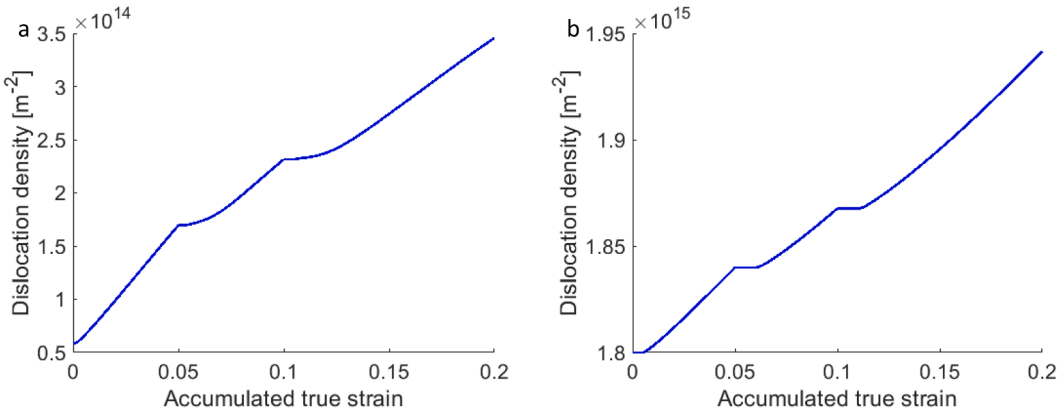

Fig. 9. Evolution of total dislocation density ($\sum_s \rho^s_{tot}$) during forward tension to 0.05 strain followed by the 1st and the 2nd reversal for (a) AA6016-T4 deformed along RD and in (b) AA7021-T79 deformed along RD.

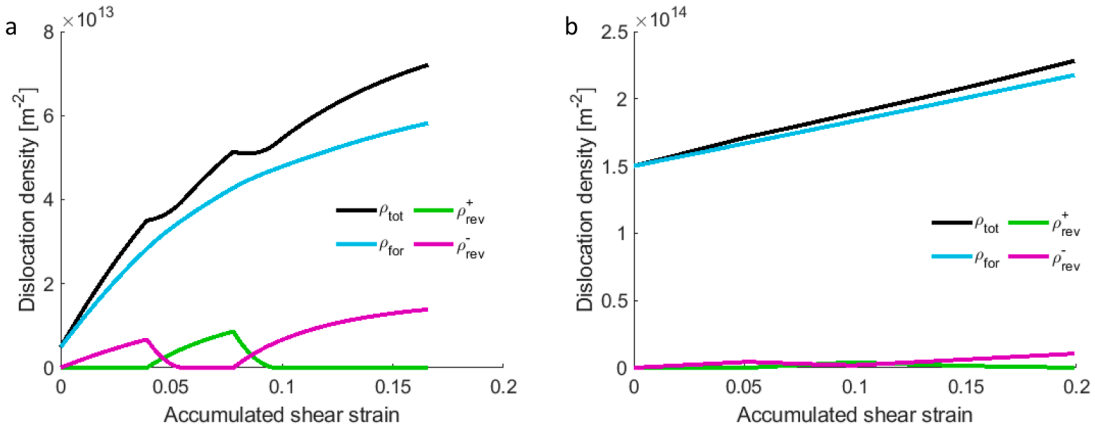

Fig. 10. Evolution of dislocation populations with the accumulated shear for a slip system with the highest activity in a randomly selected grain during forward tension to 0.05 strain followed by the 1st and the 2nd reversal along RD for (c) AA6016-T4 and (d) AA7021-T79.

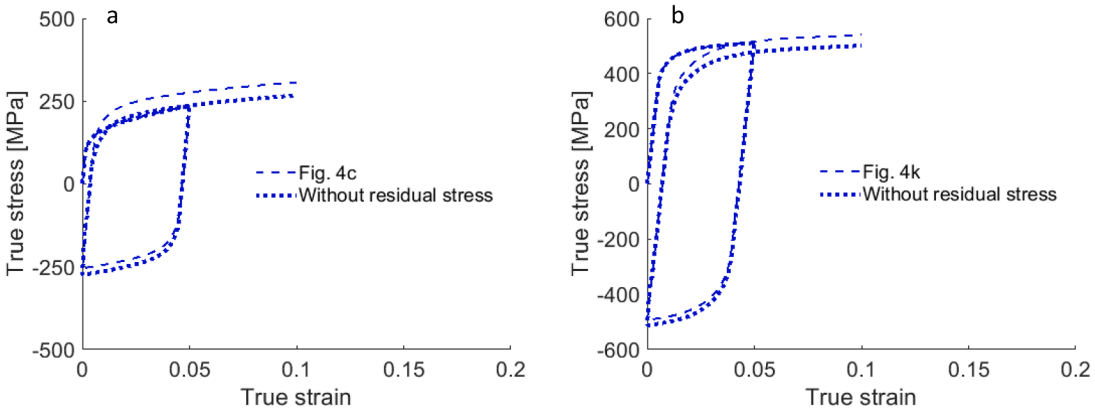

Fig. 11. Comparison of true stress–true strain response simulated with and without residual stress during forward tension to 0.05 strain followed by the 1st and the 2nd reversal along RD for (a) AA6016-T4 and (b) AA7021-T79.

Good predictions of the strain-path reversal deformation behavior of the alloys is a collective result of several distinct physical phenomena incorporated in the model. The evolution of inter-granular stress fields is the remaining phenomena the model accounts for. In general, the backstress fields have intra-granular and inter-granular sources in polycrystals. Inter-granular sources are the interactions between individual grains of different crystal orientations. As already mentioned, these effects are approximated in the EPSC formulation because every grain interacts with the averaged polycrystalline response unlike in full-field models in which grain-to-grain interaction are explicitly modeled. At zero applied stress, these inter-granular stress fields become residual stress fields Fig. 11. shows the role of residual stress in the predictions. To obtain the predictions without residual stress, grain stress is set to zero at the zero overall flow stress after the 1st and 2nd reversals. The response after the 1st reversal is controlled by the slip resistance at the end of monotonic tension pre-straining and backstress. Evidently, the inter-granular stresses govern the BE and yield differentials along with the backstresses but do not play a significant role for the nonlinear unloading. These results agree with arguments presented in (Kassner et al., 2009) that solely intra-granular backstress-based theories do not completely describe the BE. From the comparison of the curves with and without inter-granular stresses, it is evident that the inter-granular stresses are aiding plastic deformation in the reverse direction (i.e. the compression). Subsequently, the model predicts a decrease in yield stress in tension. The difference is ~40 MPa for both alloys compared to that at the end of the first tension. Similar effects of inter-granular stresses on the cyclic deformation were reported in (Li et al., 2014; Wu et al., 2005).

Given that the EPSC model has been coupled with the FEM to treat complex, non-monotonic deformation conditions in prior works, future works will focus on various metal forming simulations taking advantage of the EPSC adjusted here to capture the cyclic plasticity phenomena as these have essential implications on the accuracy of metal forming simulations, especially in accurate prediction of springback. As many of these features that were observed in the flow stresses of AA6016-T4 and AA7021-T79 are similar to those in other cubic alloys, the present model is expected to be applicable to a wider set of alloys in addition to Al alloys.

6. Conclusions

The monotonic and large strain cyclic response of AA6016-T4 and AA7021-T79 sheets was measured along the rolling and transverse directions. The data for both alloys showed the typical decreasing hardening rates during monotonic tension cycles. Upon the 1st strain path reversal, the extent of the nonlinear unloading was greater for AA7021-T79 than for AA6016-T4. The magnitude of macro-yield stress increased with the pre-strain level in monotonic tension for both alloys. As a result, the unloading deviation stress decreased, especially for the stronger AA7021-T79. The nonlinear unloading caused a prolonged elasto-plastic transition to re-yielding. The BE was evident in both alloys and increased with pre-strain and strength. Upon re-yielding, the rates of strain hardening were quickly restored. Interestingly, the strain hardening in compression was sufficient to increase to that of monotonic tension for AA7021-T79 but insufficient for AA6016-T4. As a result, AA6016-T4 exhibited a permanent softening phenomenon. Upon the 2nd strain path reversal, the hysteresis loops closed for AA7021-T79 but not for AA6016-T4. Consequently, the reloading yield stress differential under tension arose and increased with the level of pre-strain for AA6016-T4 but not for AA7021-T79. The multiple forward-reversal cyclic curves showed that the reloading softening stress and resulting ratcheting strain were small for both alloys.

The true stress-true strain data were used to calibrate and then critically validate the EPSC crystal plasticity model, which features sub-models including anisotropic elasticity, a strain-path sensitive law for the evolution of dislocation density, and a backstress law at

the slip system-level. The model reproduced the response of both alloys during monotonic and cyclic deformation to various levels of plastic pre-strains with good accuracy using a single set of parameters per alloy. Such good performances of the model were primarily a consequence of accounting for kinematic hardening at the slip system-level through the evolution law for backstress, inter-granular stresses, and dislocation annihilation reflecting the experimentally observed stagnation in the dislocation density build up upon strain reversals. Comparison of the experimental and modeling results revealed that the unloading behavior is primarily driven by backstress, the BE is governed by backstress and inter-granular stresses, and the hardening rates upon load reversals are controlled primarily by the strain-path sensitive evolution of dislocation density. Significantly, the model predicted the contrasting characteristics in the hysteresis of the alloys, such as the presence of large permanent softening and reloading yield stress differential in AA6016-T4 as compared to AA7021-T79.

CRediT authorship contribution statement

Sowmya Daroju: Software, Validation, Formal analysis, Investigation, Data curation. **Toshihiko Kuwabara:** Methodology, Formal analysis, Investigation, Writing – review & editing. **Rishabh Sharma:** Validation, Formal analysis, Investigation. **David T. Fullwood:** Investigation, Resources, Writing – review & editing, Supervision, Funding acquisition. **Michael P. Miles:** Investigation, Resources, Writing – review & editing, Supervision. **Marko Knezevic:** Conceptualization, Methodology, Software, Resources, Writing – original draft, Writing – review & editing, Supervision, Project administration, Funding acquisition.

Declaration of Competing Interest

The authors declare that they have no known competing financial interests or personal relationships that could have appeared to influence the work reported in this paper.

Acknowledgments

The authors acknowledge support from the U.S. National Science Foundation (NSF) under grant no. CMMI-1926677 (UNH) and CMMI-1926662 (BYU). The aluminum sheet alloys used for this study were supplied by Commonwealth Rolled Products.

Appendix A

This appendix presents geometry of the specimen used for the load reversal testing (Fig. A1) (Noma and Kuwabara, 2012), inverse pole figure (IPF) maps showing grain structure in the alloys (Fig. A2), IPF maps showing the deformation microstructures in alloy AA6016-T4 (Fig. A3), and texture evolution in alloy AA6016-T4 (Fig. A4).

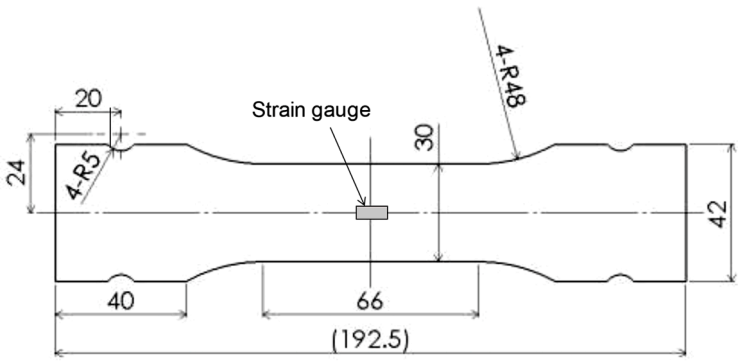

Fig. A1. Geometry of the specimen used in the tension-compression testing. Units in mm.

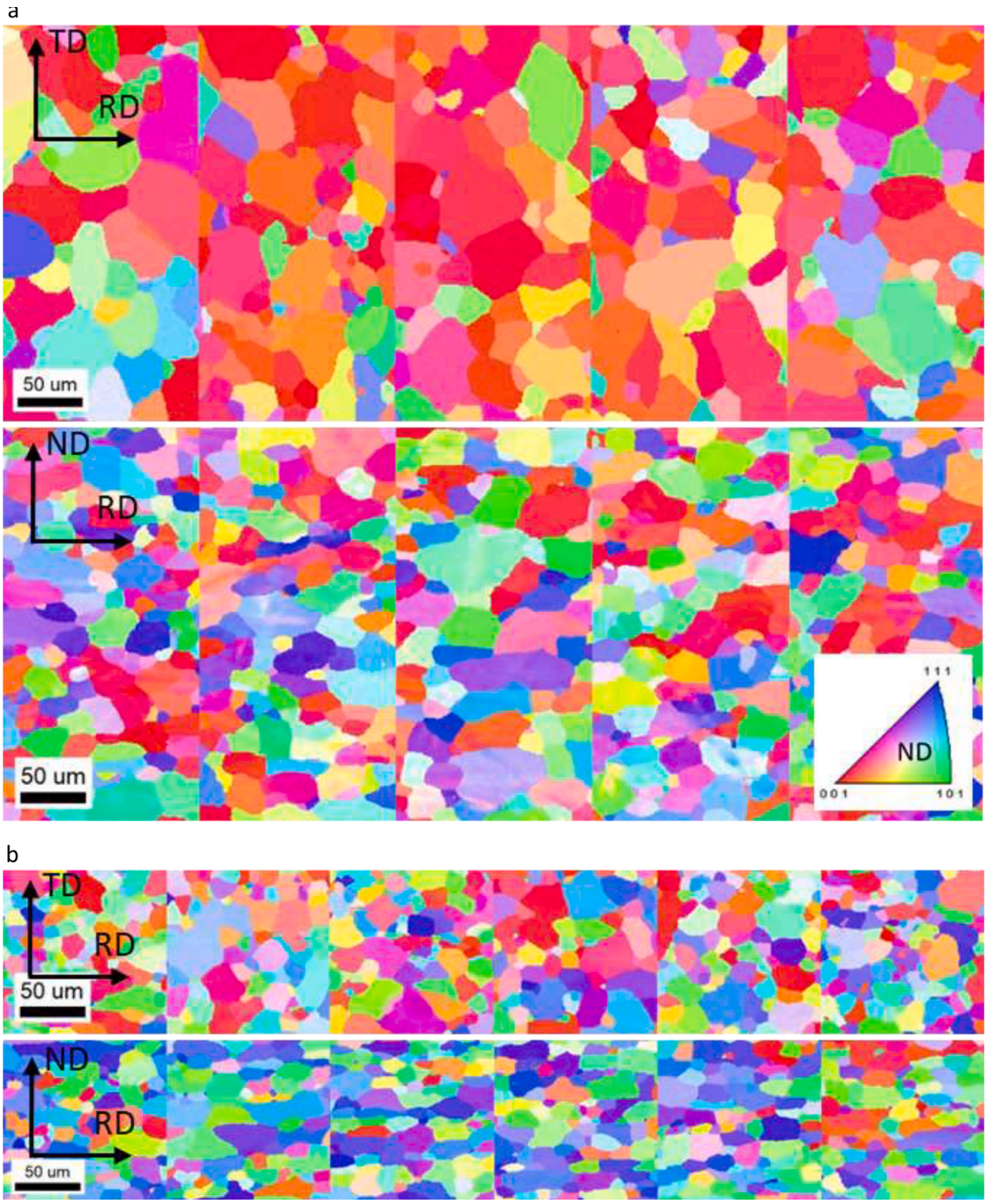

Fig. A2. IPF orientation maps for (a) AA6016-T4 and (b) AA7021-T79. Note that several different regions of virgin samples are scanned. The standard IPF triangle defines colors for the sample axis ND. Horizontal and vertical axes of the maps are indicated in the maps. Based on the maps, average grain size is 32 μm in RD, 30 μm in TD, and 18 μm in ND for AA6016-T4 and 18 μm in RD, 14 μm in ND, and 9 μm in ND for AA7021-T79.

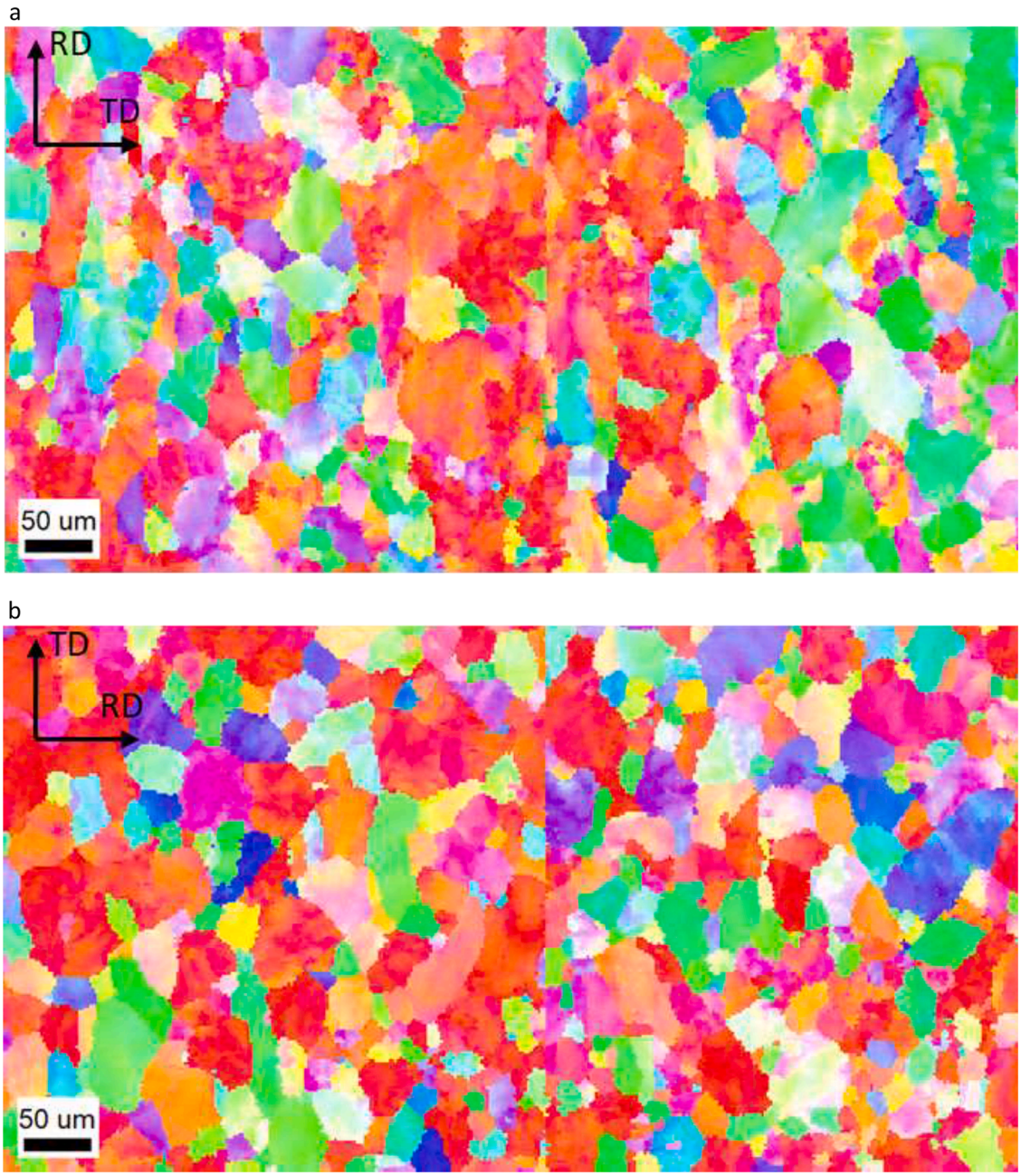

Fig. A3. IPF orientation maps for alloy AA6016-T4 after simple tension (Fig. 5): (a) to a strain of 0.2 along RD and (b) to a strain of 0.16 along TD. The standard IPF triangle defining the colors for the sample axis ND is the same as in Fig. A2.

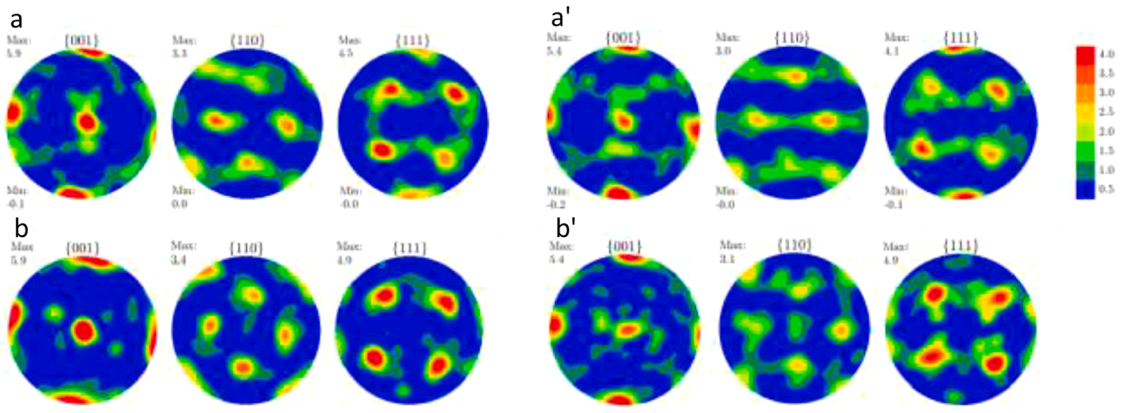

Fig. A4. Pole figures showing texture evolution in alloy AA6016-T4 after simple tension (Fig. 5): (a) measured and (a') simulated to a strain of 0.2 along RD and (b) measured and (b') simulated to a strain of 0.16 along TD.

Appendix B

Entries of the hardening matrix, $h^{ss'}$, are partial derivatives of slip resistance, Eq. (10), with respect to shearing strain on slip systems

$$h^{ss'} = \frac{\partial \tau_c^s}{\partial \gamma^{s'}} = \frac{\partial \tau_0}{\partial \gamma^{s'}} + \frac{\partial \tau_{forest}^s}{\partial \gamma^{s'}} + \frac{\partial \tau_{debris}}{\partial \gamma^{s'}} \,. \tag{B1}$$

The index s' goes over all active slip systems. Since the initial slip resistance, τ_0, is a constant its derivative vanish, while derivatives of the forest and debris contributions to slip resistance are

$$\frac{\partial \tau_{forest}^s}{\partial \gamma^{s'}} = \frac{\partial \tau_{forest}^s}{\partial \rho_{tot}^{s'}} \frac{\partial \rho_{tot}^{s'}}{\partial \gamma^{s'}} = b^a \chi \mu^a \frac{1}{2\sqrt{\sum_{s'} L^{ss'} \rho_{tot}^{s'}}} L^{ss'} \left(\frac{\partial \rho_{for}^{s'}}{\partial \gamma^{s'}} + \frac{\partial \rho_{rev}^{s'^+}}{\partial \gamma^{s'}} + \frac{\partial \rho_{rev}^{s'^-}}{\partial \gamma^{s'}} \right), \tag{B2}$$

$$\frac{\partial \tau_{debris}}{\partial \gamma^{s'}} = \frac{\partial \tau_{debris}}{\partial \rho_{deb}} \frac{\partial \rho_{deb}}{\partial \gamma^{s'}} = -k_{deb} \mu b \left(log\left(b\sqrt{\rho_{deb}} \right) + 1 \right) \frac{1}{2\sqrt{\rho_{deb}}} \frac{\partial \rho_{deb}}{\partial \gamma^{s'}}. \tag{B3}$$

The derivatives of forward, reversible, and debris dislocation densities with respect to shear strain are given in section 3.

Similarly, entries of the backstress matrix are partial derivatives of backstress given with Eq. (22) with respect to shearing strain on slip systems

$$h_{bs}^{ss'} = \frac{\partial \tau_{bs}^s}{\partial \gamma^{s'}} = \begin{cases} \dfrac{\partial \tau_{bs,sys}^s}{\partial \gamma^s} & if\ s = s' \\ 2\ \mathbf{m}^s \cdot \mathbf{m}^{s'} \dfrac{\partial \tau_{bs,sys*}^{s'}}{\partial \gamma^{s'}} & if\ s \neq s' \end{cases} \tag{B4}$$

where s' goes over set of active slip systems. Using Eq. (23), the derivative $\frac{\partial \tau_{bs,sys*}^{s'}}{\partial \gamma^{s'}}$ is

$$\frac{\partial \tau_{bs,sys*}^{s'}}{\partial \gamma^{s'}} = \begin{cases} \dfrac{\partial \tau_{bs,sys}^{s'}}{\partial \gamma^{s'}} & if\ \tau_{bs,sys}^{s'} > 0 \\ 0 & if\ \tau_{bs,sys}^{s'} > 0 \end{cases} \,. \tag{B5}$$

Finally, we provide the derivative of slip system backstress sources, $\frac{\partial \tau_{bs,sys}^s}{\partial \gamma^s}$. In the case of shearing in s^+ direction, $d\gamma^{s^+} > 0$, with $\tau_{bs}^{s^+} \geq 0$:

$$\frac{\partial \tau_{bs,sys}^{s^+}}{\partial \gamma^{s^+}} = \tau_{bs}^{sat} \nu \exp(-\nu \gamma^{s^+}), \tag{B6}$$

$$\frac{\partial \tau_{bs,sys}^{s^-}}{\partial \gamma^{s^+}} = -A \frac{\partial \tau_{bs,sys}^{s^+}}{\partial \gamma^{s^+}}. \tag{B7}$$

The derivative of slip system backstress source in case of shearing in s^+ direction, $d\gamma^{s^+} > 0$, with $\tau_{bs,sys}^{s^+} < 0$ is:

$$\frac{\partial \tau_{bs,sys}^{s^+}}{\partial \gamma^{s^+}} = \frac{(A+1)\tau_{bs}^{sat}}{\gamma_b} \exp\left(-\frac{\gamma^{s^+}}{\gamma_b}\right), \tag{B8}$$

$$\frac{\partial \tau_{bs,sys}^{s^-}}{\partial \gamma^{s^+}} = \frac{1}{A} \frac{\partial \tau_{bs,sys}^{s^+}}{\partial \gamma^{s^+}}. \tag{B9}$$

References

Abel, A., 1987. Historical perspectives and some of the main features of the Bauschinger effect. Materials Forum. Institute of Metals and Materials Australasia 11–26.

Anjabin, N., Karimi Taheri, A., Kim, H.S., 2014. Crystal plasticity modeling of the effect of precipitate states on the work hardening and plastic anisotropy in an Al–Mg–Si alloy. Comput. Mater. Sci. 83, 78–85.

Ardeljan, M., Beyerlein, I.J., McWilliams, B.A., Knezevic, M., 2016. Strain rate and temperature sensitive multi-level crystal plasticity model for large plastic deformation behavior: Application to AZ31 magnesium alloy. Int. J. Plast. 83, 90–109.

Armstrong, P.J., Frederick, C.O., 1966. A mathematical representation of multiaxial Bauschinger effect. Berkeley nuclear laboratories.

Barlat, F., Ferreira Duarte, J., Gracio, J., Lopes, A., Rauch, E., 2003. Plastic flow for non-monotonic loading conditions of an aluminum alloy sheet sample. Int. J. Plast. 19, 1215–1244.

Barrett, T.J., Eghtesad, A., McCabe, R.J., Clausen, B., Brown, D.W., Vogel, S.C., Knezevic, M., 2019. A generalized spherical harmonics-based procedure for the interpolation of partial datasets of orientation distributions to enable crystal mechanics-based simulations. Materialia 6, 100328.

Barrett, T.J., Knezevic, M., 2019. Deep drawing simulations using the finite element method embedding a multi-level crystal plasticity constitutive law: Experimental verification and sensitivity analysis. Computer Methods in Applied Mechanics and Engineering 354, 245–270.

Barrett, T.J., Knezevic, M., 2020. Modeling material behavior during continuous bending under tension for inferring the post-necking strain hardening response of ductile sheet metals: Application to DP 780 steel. International Journal of Mechanical Sciences 174, 105508.

Barrett, T.J., McCabe, R.J., Brown, D.W., Clausen, B., Vogel, S.C., Knezevic, M., 2020a. Predicting deformation behavior of α-uranium during tension, compression, load reversal, rolling, and sheet forming using elasto-plastic, multi-level crystal plasticity coupled with finite elements. J. Mech. Phys. Solids 138, 103924.

Barrett, T.J., Takagi, S., Islam, N., Kuwabara, T., Hassan, T., Kinsey, B.L., Knezevic, M., Korkolis, Y.P., 2020b. Material modeling and simulation of continuous-bending-under-tension of AA6022-T4. Journal of Materials Processing Technology, 116658.

Bate, P., Roberts, W., Wilson, D., 1981. The plastic anisotropy of two-phase aluminium alloys—I. Anisotropy in unidirectional deformation. Acta Metall 29, 1797–1814.

Bate, P., Roberts, W., Wilson, D., 1982. The plastic anisotropy of two-phase aluminium alloys—II. anisotropic behaviour in load-reversal tests. Acta Metall 30, 725–737.

Bate, P., Wilson, D., 1986a. Analysis of the Bauschinger effect. Acta Metall 34, 1097–1105.

Bate, P.S., Wilson, D.V., 1986b. Analysis of the bauschinger effect. Acta Metallurgica 34, 1097–1105.

Bauschinger, J., 1886. Über die Veränderung der Elasticitätsgrenze und Festigkeit des Eisen und Stahls durch Strecken und Quetschen, durch Erwarmen und Abkühlen und durch oftmal wiederholte Beanspruchung. Mitteilungen aus dem mechanisch-technischen Laboratorium der k. polytechnischen Schule, 1877-1836.

Beyerlein, I.J., 2008. Plastic Behavior of Metals in Reverse Straining after Large Pre-Strains. Materials Science Forum 579, 41–60.

Beyerlein, I.J., Tomé, C.N., 2008. A dislocation-based constitutive law for pure Zr including temperature effects. Int. J. Plast. 24, 867–895.

Boger, R., Wagoner, R., Barlat, F., Lee, M., Chung, K., 2005. Continuous, large strain, tension/compression testing of sheet material. Int. J. Plast. 21, 2319–2343.

Brown, G.M., 1970. Inelastic deformation of an aluminum alloy under combined stress at elevated temperature. J. Mech. Phys. Solids 18, 383–396.

Brown, L.M., Clarke, D.R., 1975. Work hardening due to internal stresses in composite materials. Acta Metallurgica 23, 821–830.

Buckley, S.N., Entwistle, K.M., 1956. The bauschinger effect in super-pure aluminum single crystals and polycrystals. Acta Metall 4, 352–361.

Chaboche, J., Rousselier, G., 1983. On the plastic and viscoplastic constitutive equations—Part I: Rules developed with internal variable concept. Journal of Pressure Vessel Technology 105, 153–158.

Chaboche, J.L., 1977. Viscoplastic constitutive equations for the description of cyclic and ansiotropic behavior of metals. In: XVIIth Polish solid mechanics conference, Bulletin de l'Académie Polonaise des Sciences, Série Sciences et Techniques, pp. 33–41.

Chaboche, J.L., 2008. A review of some plasticity and viscoplasticity constitutive theories. Int. J. Plast. 24, 1642–1693.

Chen, Z., Maekawa, S., Takeda, T., 1999. Bauschinger effect and multiaxial yield behavior of stress-reversed mild steel. Metall. Mater. Trans. A 30, 3069–3078.

Chun, B.K., Jinn, J.T., Lee, J.K., 2002. Modeling the Bauschinger effect for sheet metals, part I: theory. Int. J. Plast. 18, 571–595.

Couturier, L., Deschamps, A., De Geuser, F., Fazeli, F., Poole, W.J., 2017. An investigation of the strain dependence of dynamic precipitation in an Al-Zn-Mg-Cu alloy. Scr. Mater. 136, 120–123.

Demir, E., Raabe, D., 2010. Mechanical and microstructural single-crystal Bauschinger effects: Observation of reversible plasticity in copper during bending. Acta. Mater. 58, 6055–6063.

Devincre, B., Kubin, L., Hoc, T., 2006. Physical analyses of crystal plasticity by DD simulations. Scr. Mater. 54, 741–746.

Dietrich, L., Turski, K., 1978. New method of sheet metal compression tests. Rozp. Inz. 26.

Eghtesad, A., Barrett, T.J., Germaschewski, K., Lebensohn, R.A., McCabe, R.J., Knezevic, M., 2018a. OpenMP and MPI implementations of an elasto-viscoplastic fast Fourier transform-based micromechanical solver for fast crystal plasticity modeling. Advances in Engineering Software 126, 46–60.

Eghtesad, A., Barrett, T.J., Knezevic, M., 2018b. Compact reconstruction of orientation distributions using generalized spherical harmonics to advance large-scale crystal plasticity modeling: Verification using cubic, hexagonal, and orthorhombic polycrystals. Acta. Mater. 155, 418–432.

Eghtesad, A., Germaschewski, K., Lebensohn, R.A., Knezevic, M., 2020. A multi-GPU implementation of a full-field crystal plasticity solver for efficient modeling of high-resolution microstructures. Computer Physics Communications 254, 107231.

Eghtesad, A., Zecevic, M., Lebensohn, R.A., McCabe, R.J., Knezevic, M., 2018c. Spectral database constitutive representation within a spectral micromechanical solver for computationally efficient polycrystal plasticity modelling. Comput. Mech. 61, 89–104.

Eshelby, J.D., 1957. The determination of the elastic field of an ellipsoidal inclusion, and related problems. Proc R. Soc. Lond. A 241, 376–396.

Eskin, D.G., Kharakterova, M.L., 2001. The effect of silicon and copper on the precipitation hardnening of sheets of 6xxx series alloy. Mater. Technol. 35, 5–8.

Feather, W.G., Ghorbanpour, S., Savage, D.J., Ardeljan, M., Jahedi, M., McWilliams, B.A., Gupta, N., Xiang, C., Vogel, S.C., Knezevic, M., 2019. Mechanical response, twinning, and texture evolution of WE43 magnesium-rare earth alloy as a function of strain rate: Experiments and multi-level crystal plasticity modeling. Int. J. Plast. 120, 180–204.

Feather, W.G., Lim, H., Knezevic, M., 2020. A numerical study into element type and mesh resolution for crystal plasticity finite element modeling of explicit grain structures. Comput. Mech.

Feather, W.G., Savage, D.J., Knezevic, M., 2021. A crystal plasticity finite element model embedding strain-rate sensitivities inherent to deformation mechanisms: Application to alloy AZ31. Int. J. Plast. 143, 103031.

Feng, Z., Yoon, S.-Y., Choi, J.-H., Barrett, T.J., Zecevic, M., Barlat, F., Knezevic, M., 2020. A comparative study between elasto-plastic self-consistent crystal plasticity and anisotropic yield function with distortional hardening formulations for sheet metal forming. Mechanics of Materials 148, 103422.

Feng, Z., Zecevic, M., Knezevic, M., 2021. Stress-assisted (γ→α′) and strain-induced (γ→ε→α′) phase transformation kinetics laws implemented in a crystal plasticity model for predicting strain path sensitive deformation of austenitic steels. Int. J. Plast. 136, 102807.
Ferreri, N.C., Feng, Z., Savage, D.J., Brown, D.W., Clausen, B., Sisneros, T.A., Knezevic, M., 2022. In-situ high-energy X-ray diffraction and crystal plasticity modeling to predict the evolution of texture, twinning, lattice strains and strength during loading and reloading of beryllium. Int. J. Plast. 150, 103217.
Ghorbanpour, S., Alam, M.E., Ferreri, N.C., Kumar, A., McWilliams, B.A., Vogel, S.C., Bicknell, J., Beyerlein, I.J., Knezevic, M., 2020. Experimental characterization and crystal plasticity modeling of anisotropy, tension-compression asymmetry, and texture evolution of additively manufactured Inconel 718 at room and elevated temperatures. Int. J. Plast. 125, 63–79.
Ghorbanpour, S., Zecevic, M., Kumar, A., Jahedi, M., Bicknell, J., Jorgensen, L., Beyerlein, I.J., Knezevic, M., 2017. A crystal plasticity model incorporating the effects of precipitates in superalloys: Application to tensile, compressive, and cyclic deformation of Inconel 718. Int. J. Plast. 99, 162–185.
Gough, H., Hanson, D., Wright, S., 1927. The Behaviour of Single Crystals of Aluminium under Static and Repeated Stresses. Philosophical Transactions of the Royal Society of London. Series A, Containing Papers of a Mathematical or Physical Character 1–30.
Gracio, J.J., Barlat, F., Rauch, E.F., Jones, P.T., Neto, V.F., Lopes, A.B., 2004. Artificial aging and shear deformation behaviour of 6022 aluminium alloy. Int. J. Plast. 20, 427–445.
Greetham, G., Honeycombe, R., 1960. The deformation of single crystals of aluminum 4.5-percent copper alloy. Journal of the Institute of Metals 89, 13–21.
Hasegawa, T., Yakou, T., Karashima, S., 1975a. Deformation behaviour and dislocation structures upon stress reversal in polycrystalline aluminium. Materials Science and Engineering 20, 267–276.
Hasegawa, T., Yakou, T., Karashima, S., 1975b. Deformation behaviour and dislocation structures upon stress reversal in polycrystalline aluminium. Materials Science and Engineering 20, 267–276.
Hoc, T., Devincre, B., Kubin, L., 2004. Deformation stage I of FCC crystals: Constitutive modelling. In: 25 th Riso International Symposium on Materials Science 2004, pp. 43–59.
Hu, Z., Rauch, E.F., Teodosiu, C., 1992. Work-hardening behavior of mild steel under stress reversal at large strains. Int. J. Plast. 8, 839–856.
Iftikhar, C.M.A., Li, Y.L., Kohar, C.P., Inal, K., Khan, A.S., 2021. Evolution of subsequent yield surfaces with plastic deformation along proportional and non-proportional loading paths on annealed AA6061 alloy: Experiments and crystal plasticity finite element modeling. Int. J. Plast. 143, 102956.
Jaafar, A., Rahmat, A., Zainol, l., Hussain, Z., 2012. Effects of Composition on the Mechanical Properties and Microstructural Development of Dilute 6000 Series Alloys. Journal of Applied Science 12, 775–780.
Jahedi, M., Knezevic, M., Paydar, M., 2015. High-Pressure Double Torsion as a Severe Plastic Deformation Process: Experimental Procedure and Finite Element Modeling. J. Mater. Eng. Perform. 24, 1471–1482.
Jahedi, M., Paydar, M.H., Zheng, S., Beyerlein, I.J., Knezevic, M., 2014. Texture evolution and enhanced grain refinement under high-pressure-double-torsion. Mater. Sci. Eng. A 611, 29–36.
Kalidindi, S.R., Bronkhorst, C.A., Anand, L., 1992. Crystallographic texture evolution in bulk deformation processing of FCC metals. J. Mech. Phys. Solids 40, 537–569.
Kalidindi, S.R., Duvvuru, H.K., Knezevic, M., 2006. Spectral calibration of crystal plasticity models. Acta. Mater. 54, 1795–1804.
Kassner, M.E., Geantil, P., Levine, L.E., 2013. Long range internal stresses in single-phase crystalline materials. International Journal of Plasticity 45, 44–60.
Khadyko, M., Dumoulin, S., Cailletaud, G., Hopperstad, O.S., 2016. Latent hardening and plastic anisotropy evolution in AA6060 aluminium alloy. Int. J. Plast. 76, 51–74.
Kitayama, K., Tomé, C.N., Rauch, E.F., Gracio, J.J., Barlat, F., 2013a. A crystallographic dislocation model for describing hardening of polycrystals during strain path changes. Application to low carbon steels. International Journal of Plasticity in press.
Kitayama, K., Tomé, C.N., Rauch, E.F., Gracio, J.J., Barlat, F., 2013b. A crystallographic dislocation model for describing hardening of polycrystals during strain path changes. Application to low carbon steels. International Journal of Plasticity 46, 54–69.
Knezevic, M., Al-Harbi, H.F., Kalidindi, S.R., 2009. Crystal plasticity simulations using discrete Fourier transforms. Acta. Mater. 57, 1777–1784.
Knezevic, M., Beyerlein, I.J., 2018. Multiscale Modeling of Microstructure-Property Relationships of Polycrystalline Metals during Thermo-Mechanical Deformation. Advanced Engineering Materials 20, 1700956.
Knezevic, M., Beyerlein, I.J., Brown, D.W., Sisneros, T.A., Tomé, C.N., 2013a. A polycrystal plasticity model for predicting mechanical response and texture evolution during strain-path changes: Application to beryllium. Int. J. Plast. 49, 185–198.
Knezevic, M., Crapps, J., Beyerlein, I.J., Coughlin, D.R., Clarke, K.D., McCabe, R.J., 2016. Anisotropic modeling of structural components using embedded crystal plasticity constructive laws within finite elements. International Journal of Mechanical Sciences 105, 227–238.
Knezevic, M., Jahedi, M., Korkolis, Y.P., Beyerlein, I.J., 2014. Material-based design of the extrusion of bimetallic tubes. Comput. Mater. Sci. 95, 63–73.
Knezevic, M., Kalidindi, S.R., 2007. Fast computation of first-order elastic-plastic closures for polycrystalline cubic-orthorhombic microstructures. Comput. Mater. Sci. 39, 643–648.
Knezevic, M., Kalidindi, S.R., Fullwood, D., 2008a. Computationally efficient database and spectral interpolation for fully plastic Taylor-type crystal plasticity calculations of face-centered cubic polycrystals. Int. J. Plast. 24, 1264–1276.
Knezevic, M., Kalidindi, S.R., Mishra, R.K., 2008b. Delineation of first-order closures for plastic properties requiring explicit consideration of strain hardening and crystallographic texture evolution. Int. J. Plast. 24, 327–342.
Knezevic, M., Landry, N.W., 2015. Procedures for reducing large datasets of crystal orientations using generalized spherical harmonics. Mechanics of Materials 88, 73–86.
Knezevic, M., Levinson, A., Harris, R., Mishra, R.K., Doherty, R.D., Kalidindi, S.R., 2010. Deformation twinning in AZ31: Influence on strain hardening and texture evolution. Acta. Mater. 58, 6230–6242.
Knezevic, M., McCabe, R.J., Lebensohn, R.A., Tomé, C.N., Liu, C., Lovato, M.L., Mihaila, B., 2013b. Integration of self-consistent polycrystal plasticity with dislocation density based hardening laws within an implicit finite element framework: Application to low-symmetry metals. J. Mech. Phys. Solids 61, 2034–2046.
Knezevic, M., Poulin, C.M., Zheng, X., Zheng, S., Beyerlein, I.J., 2019. Strengthening of alloy AA6022-T4 by continuous bending under tension. Mater. Sci. Eng. A 758, 47–55.
Knockaert, R., Chastel, Y., Massoni, E., 2000. Rate-independent crystalline and polycrystalline plasticity, application to FCC materials. International Journal of Plasticity 16, 179–198.
Kocks, U.F., Franciosi, P., Kawai, M., 1991. A Forest Model of Latent Hardening and its Application to Polycrystal Deformations. Textures and Microstructures 14, 1103–1114.
Kocks, U.F., Tomé, C.N., Wenk, H.-R., 1998. Texture and Anisotropy. Cambridge University Press, Cambridge, UK.
Kuwabara, T., Kumano, Y., Ziegelheim, J., Kurosaki, I., 2009. Tension–compression asymmetry of phosphor bronze for electronic parts and its effect on bending behavior. Int. J. Plast. 25, 1759–1776.
Kuwabara, T., Nagata, K., Nakako, T., 2001. Measurement and analysis of the Bauschinger effect of sheet metals subjected to in plane stress reversals. Proceedings of AMPT 1, 407–412.
Lavrentev, F.F., 1980. The type of dislocation interaction as the factor determining work hardening. Materials Science and Engineering 46, 191–208.
Lebensohn, R.A., Kanjarla, A.K., Eisenlohr, P., 2012. An elasto-viscoplastic formulation based on fast Fourier transforms for the prediction of micromechanical fields in polycrystalline materials. Int. J. Plast. 32-33, 59–69.
Lebensohn, R.A., Tomé, C.N., 1993. A self-consistent anisotropic approach for the simulation of plastic deformation and texture development of polycrystals: Application to zirconium alloys. Acta Metall. Mater. 41, 2611–2624.
Lebensohn, R.A., Zecevic, M., Knezevic, M., McCabe, R.J., 2016. Average intragranular misorientation trends in polycrystalline materials predicted by a viscoplastic self-consistent approach. Acta. Mater. 104, 228–236.
Lentz, M., Klaus, M., Beyerlein, I.J., Zecevic, M., Reimers, W., Knezevic, M., 2015. In situ X-ray diffraction and crystal plasticity modeling of the deformation behavior of extruded Mg–Li–(Al) alloys: An uncommon tension–compression asymmetry. Acta. Mater. 86, 254–268.

Li, L., Shen, L., Proust, G., 2014. A texture-based representative volume element crystal plasticity model for predicting Bauschinger effect during cyclic loading. Materials Science and Engineering: A 608, 174–183.
Lipinski, P., Berveiller, M., 1989. Elastoplasticity of micro-inhomogeneous metals at large strains. Int. J. Plast. 5, 149–172.
Lopes, A.B., Rauch, E.F., Gracio, J.J., 1999. Textural vs structural plastic instabilities in sheet metal forming. Acta. Mater. 47, 859–866.
McDowell, D.L., 1992. A nonlinear kinematic hardening theory for cyclic thermoplasticity and thermoviscoplasticity. Int. J. Plast. 8, 695–728.
Mecking, H., Kocks, U.F., 1981. Kinetics of flow and strain-hardening. Acta Metall. Mater. 29, 1865–1875.
Miao, W.F., Laughlin, D.E., 1999. Precipitation hardening in aluminum alloy 6022. Scripta Materialia 40, 873–878.
Mirihanage, W.U., Robson, J.D., Mishra, S., Hidalgo-Manrique, P., da Fonseca, J.Q., Daniel, C.S., Prangnell, P.B., Michalik, S., Magdysyuk, O.V., Connolley, T., Drakopoulos, M., 2021. Direct observation of the dynamic evolution of precipitates in aluminium alloy 7021 at high strain rates via high energy synchrotron X-rays. Acta. Mater. 205, 116532.
Mompiou, F., Caillard, D., Legros, M., Mughrabi, H., 2012. In situ TEM observations of reverse dislocation motion upon unloading in tensile-deformed UFG aluminium. Acta. Mater. 60, 3402–3414.
Mughrabi, H., 1983. Dislocation wall and cell structures and long-range internal stresses in deformed metal crystals. Acta Metall 31, 1367–1379.
Nagtegaal, J.C., Veldpaus, F.E., 1984. On the implementation of finite strain plasticity equations in a numerical model. Numerical methods in industrial forming processes 351–371.
Neil, C.J., Wollmershauser, J.A., Clausen, B., Tomé, C.N., Agnew, S.R., 2010. Modeling lattice strain evolution at finite strains and experimental verification for copper and stainless steel using in situ neutron diffraction. Int. J. Plast. 26, 1772–1791.
Nieh, T.G., Nix, W.D., 1986. Unloading yield effects in aluminum alloys. Metallurgical transactions. A, Physical metallurgy and materials science 17 A 121–126.
Noma, N., Kuwabara, T., 2012. Specimen geometry optimization for in-plane reverse loading test of sheet metal and experimental validation. Steel Research International Special Edition: Metal Forming 1283–1286, 2012.
Ohno, N., 1982. A Constitutive Model of Cyclic Plasticity With a Nonhardening Strain Region. J. Appl. Mech. 49 (4), 721–727.
Ohno, N., Kachi, Y., 1986. A Constitutive Model of Cyclic Plasticity for Nonlinear Hardening Materials. J. Appl. Mech. 53 (2), 395–403.
Ohno, N., Nakamoto, H., Morimatsu, Y., Okumura, D., 2021. Modeling of cyclic hardening and evaluation of plastic strain range in the presence of pre-loading and ratcheting. Int. J. Plast. 145, 103074.
Orowan, E., 1948. Discussion on internal stresses, Symposium on internal stresses in metals and alloys. Institute of Metals London 451–453.
Orowan, E., 1959. Causes and Effects of Internal Stresses. In: Rassweiler, G.M., Grube, W.L. (Eds.), General Motors Symposium. Elsevier, Amsterdam, pp. 59–80.
Pavlina, E., Lee, M.-G., Barlat, F., 2015. Observations on the Nonlinear Unloading Behavior of Advanced High Strength Steels. Metall. Mater. Trans. A 46, 18–22.
Peeters, B., Seefeldt, M., Teodosiu, C., Kalidindi, S.R., Van Houtte, P., Aernoudt, E., 2001. Work-hardening/softening behaviour of b.c.c. polycrystals during changing strain paths: I. An integrated model based on substructure and texture evolution, and its prediction of the stress-strain behaviour of an IF steel during two-stage strain paths. Acta. Mater. 49, 1607–1619.
Poulin, C.M., Barrett, T.J., Knezevic, M., 2020a. Inferring Post-Necking Strain Hardening Behavior of Sheets by a Combination of Continuous Bending Under Tension Testing and Finite Element Modeling. Experimental Mechanics 60, 459–473.
Poulin, C.M., Korkolis, Y.P., Kinsey, B.L., Knezevic, M., 2019. Over five-times improved elongation-to-fracture of dual-phase 1180 steel by continuous-bending-under-tension. Mater. Des. 161, 95–105.
Poulin, C.M., Vogel, S.C., Korkolis, Y.P., Kinsey, B.L., Knezevic, M., 2020b. Experimental studies into the role of cyclic bending during stretching of dual-phase steel sheets. International Journal of Material Forming 13, 393–408.
Prabhu, T.R., 2015. An Overview of High-Performance Aircraft Structural Al Alloy-AA7085. Acta Metall. Sin. (Engl. Lett.) 28, 909–921.
Risse, M., Lentz, M., Fahrenson, C., Reimers, W., Knezevic, M., Beyerlein, I.J., 2017. Elevated Temperature Effects on the Plastic Anisotropy of an Extruded Mg-4 Wt Pct Li Alloy: Experiments and Polycrystal Modeling. Metall. Mater. Trans. A 48, 446–458.
Riyad, I.A., Feather, W.G., Vasilev, E., Lebensohn, R.A., McWilliams, B.A., Pilchak, A.L., Knezevic, M., 2021. Modeling the role of local crystallographic correlations in microstructures of Ti-6Al-4V using a correlated structure visco-plastic self-consistent polycrystal plasticity formulation. Acta. Mater. 203, 116502.
Sauzay, M., 2008. Analytical modelling of intragranular backstresses due to deformation induced dislocation microstructures. Int. J. Plast. 24, 727–745.
Savage, D.J., Feng, Z., Knezevic, M., 2021. Identification of crystal plasticity model parameters by multi-objective optimization integrating microstructural evolution and mechanical data. Computer Methods in Applied Mechanics and Engineering 379, 113747.
Seeger, A., 1957. Glide and work hardening in face-centered cubic and hexagonal close-packed metals. In: Fisher, J.C. (Ed.), Dslocations and Mechanical Properties of Cryslals. Wiley, New York, p. 243 p. p.
Segurado, J., Lebensohn, R.A., Llorca, J., Tomé, C.N., 2012. Multiscale modeling of plasticity based on embedding the viscoplastic self-consistent formulation in implicit finite elements. Int. J. Plast. 28, 124–140.
Sehitoglu, H., Foglesong, T., Maier, H.J., 2005. Precipitate effects on the mechanical behavior of aluminum copper alloys: Part II. Modeling. Metall. Mater. Trans. A 36, 763–770.
Smith, A., Chen, Z., Lee, J.Y., Lee, M.G., Wagoner, R.H., 2014. Effective method for fitting complex constitutive equations. Int. J. Plast. 58, 100–119.
Sritharan, T., Chandel, R.S., 1997. Phenomena in interrupted tensile tests of heat treated aluminium alloy 6061. Acta. Mater. 45, 3155–3161.
Stout, M., Rollett, A., 1990. Large-strain Bauschinger effects in fcc metals and alloys. Metall. Mater. Trans. A 21, 3201–3213.
Szczepiński, W., 1990. Experimental methods in mechanics of solids. Elsevier.
Tan, Z., Magnusson, C., Persson, B., 1994. The Bauschinger effect in compression-tension of sheet metals. Mater. Sci. Eng. A 183, 31–38.
Tanaka, K., Mori, T., 1970. The hardening of crystals by non-deforming particles and fibres. Acta Metallurgica 18, 931–941.
Taylor, G.I., 1938. Plastic strain in metals. Journal of the Institute of Metals 62, 307–324.
Teodosiu, C., Raphanel, J.L., 1991. Finite element simulations of large elastoplastic deformations of multicrystals. Proceedings of the International Seminar 91, 153–168. MECAMAT.
Turner, P.A., Tomé, C.N., 1994. A study of residual stresses in Zircaloy-2 with rod texture. Acta Metall. Mater. 42, 4143–4153.
Verma, R.K., Kuwabara, T., Chung, K., Haldar, A., 2011. Experimental evaluation and constitutive modeling of non-proportional deformation for asymmetric steels. Int. J. Plast. 27, 82–101.
Wagoner, R.H., Lim, H., Lee, M.-G., 2013. Advanced Issues in springback. Int. J. Plast. 45, 3–20.
Wen, W., Borodachenkova, M., Tomé, C.N., Vincze, G., Rauch, E.F., Barlat, F., Grácio, J.J., 2015. Mechanical behavior of Mg subjected to strain path changes: Experiments and modeling. International Journal of Plasticity 73, 171–183.
Weng, G.J., 1979. Kinematic hardening rule in single crystals. International Journal of Solids and Structures 15, 861–870.
Weng, G.J., 1980. Constitutive equations of single crystals and polycrystalline aggregates under cyclic loading. International Journal of Engineering Science 18, 1385–1397.
Wilson, D.V., Bate, P.S., 1986. Reversibility in the work hardening of spheroidised steels. Acta Metall 34, 1107–1120.
Wilson, D.V., Zandrahimi, M., Roberts, W.T., 1990. Effects of changes in strain path on work-hardening in CP aluminium and an Al-Cu-Mg alloy. Acta Metall. Mater. 38, 215–226.
Wollmershauser, J.A., Clausen, B., Agnew, S.R., 2012. A slip system-based kinematic hardening model application to in situ neutron diffraction of cyclic deformation of austenitic stainless steel. Int. J. Fatigue 36, 181–193.
Wu, P.D., MacEwen, S.R., Lloyd, D.J., Jain, M., Tugcu, P., Neale, K.W., 2005. On pre-straining and the evolution of material anisotropy in sheet metals. International Journal of Plasticity 21, 723–739.
Yoshida, F., Uemori, T., Fujiwara, K., 2002. Elastic–plastic behavior of steel sheets under in-plane cyclic tension–compression at large strain. Int. J. Plast. 18, 633–659.
Zang, S.-l., Lee, M.-g., Hoon Kim, J., 2013. Evaluating the significance of hardening behavior and unloading modulus under strain reversal in sheet springback prediction. International Journal of Mechanical Sciences 77, 194–204.

Zecevic, M., Beyerlein, I.J., Knezevic, M., 2017a. Coupling elasto-plastic self-consistent crystal plasticity and implicit finite elements: Applications to compression, cyclic tension-compression, and bending to large strains. Int. J. Plast. 93, 187–211.
Zecevic, M., Beyerlein, I.J., Knezevic, M., 2018a. Activity of pyramidal I and II <c+a>slip in Mg alloys as revealed by texture development. J. Mech. Phys. Solids 111, 290–307.
Zecevic, M., Knezevic, M., 2015. A dislocation density based elasto-plastic self-consistent model for the prediction of cyclic deformation: Application to Al6022-T4. Int. J. Plast. 72, 200–217.
Zecevic, M., Knezevic, M., 2017. Modeling of Sheet Metal Forming Based on Implicit Embedding of the Elasto-Plastic Self-Consistent Formulation in Shell Elements: Application to Cup Drawing of AA6022-T4. JOM 69, 922–929.
Zecevic, M., Knezevic, M., 2018a. Latent hardening within the elasto-plastic self-consistent polycrystal homogenization to enable the prediction of anisotropy of AA6022-T4 sheets. Int. J. Plast. 105, 141–163.
Zecevic, M., Knezevic, M., 2018b. A new visco-plastic self-consistent formulation implicit in dislocation-based hardening within implicit finite elements: Application to high strain rate and impact deformation of tantalum. Computer Methods in Applied Mechanics and Engineering 341, 888–916.
Zecevic, M., Knezevic, M., 2019. An implicit formulation of the elasto-plastic self-consistent polycrystal plasticity model and its implementation in implicit finite elements. Mechanics of Materials 136, 103065.
Zecevic, M., Knezevic, M., Beyerlein, I.J., McCabe, R.J., 2016a. Origin of texture development in orthorhombic uranium. Mater. Sci. Eng. A 665, 108–124.
Zecevic, M., Knezevic, M., Beyerlein, I.J., Tomé, C.N., 2015. An elasto-plastic self-consistent model with hardening based on dislocation density, twinning and de-twinning: Application to strain path changes in HCP metals. Mater. Sci. Eng. A 638, 262–274.
Zecevic, M., Knezevic, M., McWilliams, B., Lebensohn, R.A., 2020. Modeling of the thermo-mechanical response and texture evolution of WE43 Mg alloy in the dynamic recrystallization regime using a viscoplastic self-consistent formulation. Int. J. Plast. 130, 102705.
Zecevic, M., Korkolis, Y.P., Kuwabara, T., Knezevic, M., 2016b. Dual-phase steel sheets under cyclic tension–compression to large strains: Experiments and crystal plasticity modeling. J. Mech. Phys. Solids 96, 65–87.
Zecevic, M., Lebensohn, R.A., McCabe, R.J., Knezevic, M., 2018b. Modeling of intragranular misorientation and grain fragmentation in polycrystalline materials using the viscoplastic self-consistent formulation. Int. J. Plast. 109, 193–211.
Zecevic, M., Pantleon, W., Lebensohn, R.A., McCabe, R.J., Knezevic, M., 2017b. Predicting intragranular misorientation distributions in polycrystalline metals using the viscoplastic self-consistent formulation. Acta. Mater. 140, 398–410.
Zecevic, M., Roemer, T., Knezevic, M., Korkolis, Y., Kinsey, B., 2016c. Residual Ductility and Microstructural Evolution in Continuous-Bending-under-Tension of AA-6022-T4. Materials 9, 130.
Zecevic, M., Upadhyay, M.V., Polatidis, E., Panzner, T., Van Swygenhoven, H., Knezevic, M., 2019. A crystallographic extension to the Olson-Cohen model for predicting strain path dependence of martensitic transformation. Acta. Mater. 166, 386–401.
Zhou, C., LeSar, R., 2012. Dislocation dynamics simulations of the Bauschinger effect in metallic thin films. Computational Materials Science 54, 350–355.